The CCM1–CCM2 complex controls complementary functions of ROCK1 and ROCK2 that are required for endothelial integrity

Justyna Lisowska, Claudia Jasmin Rödel, Sandra Manet, Yekaterina A Miroshnikova, Cyril Boyault, Emmanuelle Planus, Richard de Mets, Hsiao-Hui Lee, Olivier Destaing, Hichem C Mertani, et al.

© 2018. Published by The Company of Biologists Ltd | Journal of Cell Science (2018) 131, jcs216093. doi:10.1242/jcs.216093

RESEARCH ARTICLE

The CCM1–CCM2 complex controls complementary functions of ROCK1 and ROCK2 that are required for endothelial integrity

Justyna Lisowska[1,2,3], Claudia Jasmin Rödel[4,*], Sandra Manet[1,2,3,*], Yekaterina A. Miroshnikova[1,2,3,*], Cyril Boyault[1,2,3], Emmanuelle Planus[1,2,3], Richard De Mets[2,5], Hsiao-Hui Lee[6], Olivier Destaing[1,2,3], Hichem Mertani[7], Gwénola Boulday[8,9,10], Elisabeth Tournier-Lasserve[8,9,10], Martial Balland[2,5], Salim Abdelilah-Seyfried[4,11], Corinne Albiges-Rizo[1,2,3,*,‡] and Eva Faurobert[1,2,3,‡]

ABSTRACT

Endothelial integrity relies on a mechanical crosstalk between intercellular and cell–matrix interactions. This crosstalk is compromised in hemorrhagic vascular lesions of patients carrying loss-of-function mutations in cerebral cavernous malformation (CCM) genes. RhoA/ROCK-dependent cytoskeletal remodeling is central to the disease, as it causes unbalanced cell adhesion towards increased cell–extracellular matrix adhesions and destabilized cell–cell junctions. This study reveals that CCM proteins directly orchestrate ROCK1 and ROCK2 complementary roles on the mechanics of the endothelium. CCM proteins act as a scaffold, promoting ROCK2 interactions with VE-cadherin and limiting ROCK1 kinase activity. Loss of CCM1 (also known as KRIT1) produces excessive ROCK1-dependent actin stress fibers and destabilizes intercellular junctions. Silencing of ROCK1 but not ROCK2 restores the adhesive and mechanical homeostasis of CCM1 and CCM2-depleted endothelial monolayers, and rescues the cardiovascular defects of *ccm1* mutant zebrafish embryos. Conversely, knocking down Rock2 but not Rock1 in wild-type zebrafish embryos generates defects reminiscent of the *ccm1* mutant phenotypes. Our study uncovers the role of the CCM1–CCM2 complex in controlling ROCK1 and ROCK2 to preserve endothelial integrity and drive heart morphogenesis. Moreover, it solely identifies the ROCK1 isoform as a potential therapeutic target for the CCM disease.

KEY WORDS: CCM, ROCK, Endothelial integrity, Mechanotransduction

INTRODUCTION

A mechanical balance between cell–cell junctions and cell–extracellular matrix (ECM) adhesions controls fundamental processes during development, tissue homeostasis and disease (Mui et al., 2016; Schroer and Merryman, 2015; Zhang and Labouesse, 2012). In the endothelium, forces generated at cell–cell and cell–ECM adhesions control blood vessel morphogenesis, stability and permeability in response to physical stimuli coming from the blood circulation and the vessel wall (Amado-Azevedo et al., 2014; Huveneers et al., 2015). Cellular forces are generated by the actomyosin cytoskeleton, which acts as a force-transmitting scaffold to control both cell–cell junctions and the cell–ECM interface (Maruthamuthu et al., 2010). A dynamic interplay between vascular endothelial (VE)-cadherin (also known as CDH5) in adherens junctions (AJs) and integrins in focal adhesions (FAs) involves small GTPases, such as Rap1 and members of the Rho family, in order to properly organize the actomyosin cytoskeleton (Citi et al., 2011). RhoA and its effector ROCK proteins are key regulators of the endothelial permeability barrier (Amado-Azevedo et al., 2014; Komarova and Malik, 2010) and increased ROCK activity is involved in numerous cardiovascular diseases (Hartmann et al., 2015; Shimokawa et al., 2016). However, the precise molecular mechanisms involved in ROCK regulation remain unclear. Interestingly, RhoA can activate the two isoforms of ROCK, ROCK1 and ROCK2, which share 65% overall identity with 92% similarity at the level of their kinase domain (Julian and Olson, 2014). Whereas it has been long-assumed that there are redundant functions between both isoforms, differential functions have emerged (Hartmann et al., 2015). However, no study has ever addressed their respective role in organizing AJs and FAs to control endothelial integrity. Major questions remain as to whether the two ROCK isoforms act in a coordinated manner to mechanically regulate the two types of adhesion sites and whether ROCK isoforms are controlled by a common regulator dictating their respective roles.

The CCM1–CCM2 complex (CCM1 is also known as KRIT1), named after the cerebral cavernous malformation disease, is a cytoplasmic molecular scaffold that controls cell–cell junctions and cell–ECM adhesions (Faurobert and Albiges-Rizo, 2010; Fischer et al., 2013). The CCM complex limits the actomyosin cytoskeleton contractility by inhibiting the RhoA–ROCK pathway, and thereby negatively regulating endothelial permeability (Borikova et al., 2010; Stockton et al., 2010; Whitehead et al., 2009). Loss-of-function mutations in CCM1- or CCM2-encoding genes in humans lead to cerebral clusters of dilated and hemorrhagic capillaries (Labauge et al., 2007) with consequences ranging from headaches, focal neurological defects to hemorrhagic stroke (Yadla et al., 2010). Abnormally elevated ROCK-dependent endothelial contractility is a hallmark of pathology caused by CCM1–CCM3 (CCM3 is also known as PDCD10) (Richardson et al., 2013;

[1]INSERM U1209, Institute for Advanced Biosciences, F-38700 La Tronche, France. [2]Université Grenoble Alpes, F-38042 Grenoble, France. [3]CNRS UMR 5309, Institute for Advanced Biosciences, F-38700 La Tronche, France. [4]Institute of Biochemistry and Biology, Potsdam University, D-14476 Potsdam, Germany. [5]CNRS UMR 5588 LIPhy, F-38041 Grenoble, France. [6]Department of Life Sciences & Institute of Genome Sciences, National Yang-Ming University, Taipei City 112, Taiwan. [7]INSERM UMR 1052, CNRS 5286 CRCL Centre Léon Bérard, F-69373 Lyon Cedex 08, France. [8]INSERM, UMR-S1161, Paris, F-75010, France. [9]University Paris Diderot, Sorbonne Paris Cité, UMR-S1161, Paris, F-75010, France. [10]AP-HP, Groupe hospitalier Saint-Louis Lariboisiere-Fernand-Widal, Paris, F-75010, France. [11]Institute of Molecular Biology, Hannover Medical School, D-30625 Hannover, Germany.
*These authors contributed equally to this work

‡Authors for correspondence (eva.faurobert@univ-grenoble-alpes.fr; corinne.albiges-rizo@univ-grenoble-alpes.fr)

J.L., 0000-0002-5562-0835; Y.A.M., 0000-0001-9771-4963; C.A.-R., 0000-0002-6333-4150; E.F., 0000-0002-2714-8537

Received 29 January 2018; Accepted 3 July 2018

Journal of Cell Science (2018) 131, jcs216093. doi:10.1242/jcs.216093

Shenkar et al., 2015; Stockton et al., 2010), and increasing literature correlates this increased contractility with the genesis of CCM lesions (Fisher et al., 2015; Gibson et al., 2015; McDonald et al., 2012; Zhou et al., 2016). Inhibition of ROCK activity in *ccm* mouse models has proven to limit formation of brain lesions and maturation as well as iron deposition, a marker of hemorrhage (McDonald et al., 2012; Shenkar et al., 2017). This demonstrates the crucial role for ROCK activation in CCM lesion formation and designates ROCK as a major potential therapeutic target (Borikova et al., 2010; McDonald et al., 2012; Richardson et al., 2013; Shenkar et al., 2017; Stockton et al., 2010). Silencing of CCM1 or CCM2 causes numerous ROCK-dependent transversal actin stress fibers associated with an increased number of FAs and destabilized cell–cell junctions (Faurobert et al., 2013; Whitehead et al., 2009). It has been shown that the CCM1–CCM2 complex stimulates the formation of VE-cadherin-dependent junctions upon Rap1 activation (Glading and Ginsberg, 2010; Glading et al., 2007) and inhibits the formation of β1 integrin-dependent FAs through stabilization of ICAP-1 (also known as ITGB1BP1), a negative regulator of β1 integrin (Faurobert et al., 2013). However, how the CCM1–CCM2 complex is able to fine-tune cellular forces to control both AJ and FA formation remains unclear.

To better understand the mechanisms associated with CCM lesion pathogenesis, we sought to define the specific contributions of ROCK1 and ROCK2 downstream of the CCM complex. Here, we reveal that ROCK1 and ROCK2 are both required to preserve the mechanical endothelial homeostasis by acting in complementary ways on actomyosin organization. Importantly, we demonstrate the key role of CCM1 in orchestrating the functions of the ROCKs through the recruitment of ROCK2 to VE-cadherin complexes and the inhibition of ROCK1 kinase activity. Overactivation of ROCK1 is instrumental in mediating the increased adhesion to ECM and destabilized cell–cell junctions in CCM-depleted cells. Indeed, silencing of ROCK1 but not of ROCK2, restored cortical actin organization *in vitro* and rescued cardiac cushions and ventricular chamber formation in *ccm1* zebrafish mutant embryos. Instead, knocking down of Rock2, but not Rock1, provoked heart morphogenesis defects comparable to the *ccm1* phenotypes in wild-type (WT) embryos. Taken together, our results demonstrate that a tight control of ROCK1 and ROCK2 functions by the CCM1–CCM2 complex is mandatory to preserve endothelial integrity. Finally, they indicate the need for a specific therapeutic treatment that is not based on a generic ROCK inhibitor but rather specifically targets ROCK1.

RESULTS

The adhesive and actomyosin cytoskeleton defects upon CCM1 or CCM2 loss are phenocopied by ROCK2 loss

Since upregulation of RhoA activation and ROCK signaling pathway is a key molecular feature of the pathogenic process of the human CCM disease, we sought to perform an in-depth analysis of the contribution of the two isoforms ROCK1 and ROCK2. Since CCM lesions mainly occur in cerebral microvessels, we first confirmed that both ROCK isoforms were present in hCMEC/D3 cells, an endothelial cell line derived from human brain capillaries (Weksler et al., 2005) as well as in human umbilical vein endothelial cells (HUVECs) (Fig. S1A).

We examined the contribution of each ROCK isoform to the architecture of the actin cytoskeleton and to the assembly of FAs and AJs. To this aim, we analyzed HUVECs or hCMEC/D3 cells expressing either one of the isoforms by silencing its counterpart. In addition, we compared their phenotype to that of cells depleted for CCM1 or CCM2. Silencing of the proteins was validated by western blotting (Fig. S1B,C) or by quantitative (Q)-PCR (Fig. S1D).

We first analyzed cell morphology and the actin architecture during the early (within 1 h) process of adhesion in sparsely plated HUVECs that do not form AJs. After 1 h of spreading on fibronectin (FN), most of the cells were still round. Control-depleted HUVECs (siCT) had a dense cortical actomyosin rim (Fig. 1A). ROCK1 or ROCK2 depletion (siROCK1 and siROCK2, respectively) led to very different acto-adhesive phenotypes. When ROCK2 was expressed alone upon ROCK1 silencing, cells displayed a wider cortical actin rim in which the actin arcs appeared thinner and less packed that in control or ROCK2-depleted cells (Fig. 1A,B). Concomitantly, cells displayed more β1 integrin-dependent focal complexes at the cell border than did control- or ROCK2-depleted HUVECs, and fewer FAs at distances >5 µm from the cell border (i.e. underneath cells) (Fig. 1C–E). This is indicative of a defect in FA maturation as observed in Lock et al. (Lock and Hotchin, 2009). By contrast, when ROCK1 was expressed alone upon ROCK2 silencing, the cortical F-actin rim contained numerous α-actinin-stained dorsal ruffles that were not present in control- or ROCK1-silenced HUVECs and fewer F-actin arcs (Fig. 1A). Moreover, these cells expressed ventral actin cables that were connected to bigger β1-integrin FAs. These FAs were localized more centrally underneath the cell body than in control cells (Fig. 1C,E).

Remarkably, depletion of ROCK2, but not ROCK1, phenocopied the effects of CCM1 or CCM2 loss on F-actin and β1-integrin FA organization (Fig. 1A–E; Fig. S2A,B,D,E). After 72 h of culture at confluency, control and ROCK1-silenced HUVECs adopted a honeycomb-like shape supported by a cortical actomyosin cytoskeleton stained for phosphorylated MYL2 (denoted pMLC) (Fig. 1F). A thicker VE-cadherin-positive compartment was observed in monolayers expressing only ROCK2, which correlated with a thicker honeycomb cortical actomyosin ring (Fig. 1H,I). In contrast ROCK2-depleted HUVEC, like CCM1- or CCM2-depleted cells, were elongated as they expressed pMLC-labeled transversal actin stress fibers and no cortical F-actin (Fig. 1F; Fig. S2C). Cells displaying transversal stress fibers were three times more numerous upon ROCK2, CCM1 or CCM2 depletion than upon control or ROCK1 depletion (Fig. 1G; Fig. S2D). This was correlated with a thinning of the AJ compared to control (Fig. 1H,I; Fig. S2C,F). Similar results were obtained with the brain-derived hCMEC/D3 cells (Fig. S2G, S2H). Individual siRNA targeting ROCK1 and ROCK2, whose efficacy was shown in Fig. S1H, gave comparable phenotypes to that obtained with the ROCK1 and ROCK2 smartpool siRNA at early spreading time-points (Fig. S1E,G) as well as after 72 h of confluency (Fig. S1F), confirming these results.

Taken together, the above data show that ROCK1 and ROCK2 bear distinct but complementary roles for setting up the actomyosin cytoskeleton and maintaining the adhesive homeostasis between AJs and FAs. ROCK2 favors the formation of the cortical actin arcs and positively regulates AJs, while ROCK1 is required for the contraction of the actin arcs and the formation of ventral stress fibers, favoring FA maturation. Interestingly, depletion of ROCK2 but not of ROCK1 generates a similar unbalanced adhesive phenotype toward destabilization of AJs and increased FA size and number as observed when the CCM1–CCM2 complex is missing.

CCM1 controls ROCK2 recruitment to VE-cadherin and inhibits ROCK1 kinase activity

Our finding that ROCK2 loss phenocopies CCM1 loss suggested a functional link between the two proteins. We first looked whether

Journal of Cell Science (2018) 131, jcs216093. doi:10.1242/jcs.216093

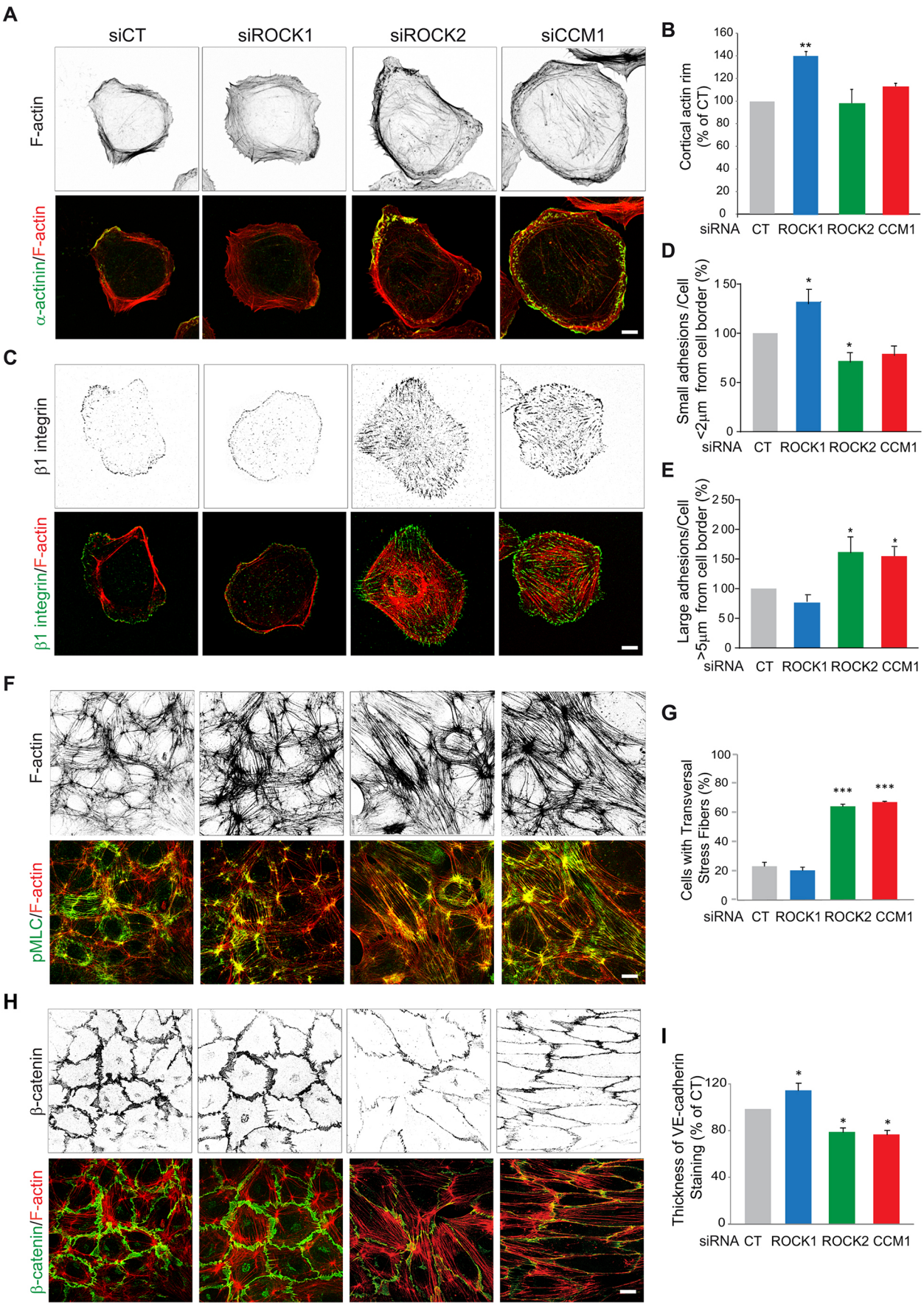

Fig. 1. See next page for legend.

Journal of Cell Science (2018) 131, jcs216093. doi:10.1242/jcs.216093

Fig. 1. ROCK2 loss phenocopies the acto-adhesive machinery defects of CCM1-depleted HUVECs. (A) Representative immunofluorescence images of F-actin (gray) and merged images with α-actinin in sparsely plated siRNA-transfected HUVECs after 1 h of spreading on 5 µg/ml FN. (B) Quantification of the ratio of cortical actin rim area to total cell area expressed as a percentage of that in the siCT condition. Error bars are s.e.m. (n=4 except for siCCM1 where n=3). (C) Representative immunofluorescence images of activated β1 integrin (gray), and merged images with F-actin, of sparsely plated siRNA-transfected HUVECs after spreading on 5 µg/ml FN for 1 h. Quantifications of the percentage of adhesion plaques per cell smaller than 0.5 µm^2 and at less than 2 µm from the cell border (D) and of the percentage of adhesion plaques per cell larger than 0.5 µm^2 at more than 5 µm from the cell border (E) were performed on 20 cells per condition, with between 200 and 800 adhesive structures counted per each cell. Error bars, s.e.m. (n=2). (F) Representative immunofluorescence images of F-actin (gray) and merged immunofluorescent images with pMLC after 72 h of culture at confluency. (G) Quantification of the percentage of cells with transversal stress fibers on 100 cells per condition. Error bars, s.e.m. (n=4). (H) Representative immunofluorescence images of β-catenin (gray) and merged images with F-actin of confluent siRNA-transfected HUVECs cultured for 72 h on 20 µg/ml FN-coated coverslips at confluency. (I) Intercellular adhesion integrity in HUVECs was assessed by quantifying the VE-cadherin thickness obtained from immunofluorescence staining of VE-cadherin, presented as percentage of control. Error bars, s.e.m. (n=4, except for ROCK1 and ROCK2 where n=3). The CT and CCM1 data are also shown in Fig. 3E. *P<0.05; **P<0.005; ***P<0.0005 (one-way ANOVA with Dunnett's multiple comparisons post-test). Scale bars: 10 µm. CT, control.

CCM1 loss impacts on the level of ROCK2 protein, and found no statistical difference between control- and CCM1-silenced HUVECs in the time-frame of these cellular assays (Fig. 2A). More globally, silencing of either one of CCM1, ROCK1 or ROCK2 had no impact on the level of the others (Fig. 2A; Fig. S1B).

CCM1 is recruited via β-catenin to cell–cell junctions where it stabilizes junctional integrity (Glading and Ginsberg, 2010). We first checked whether junctional destabilization upon depletion of CCM1 or ROCK2 could result from a lower cell surface expression of VE-cadherin. We observed instead a slight increase of the VE-cadherin amount at the cell surfaces under these conditions, ruling out this hypothesis (Fig. 2B). Interestingly, we showed that ROCK2 specifically co-immunoprecipitated with β-catenin, whereas ROCK1 did not, consistent with a requirement for ROCK2 to preserve intercellular junctions (Fig. 2C). CCM1 was required for ROCK2 recruitment to β-catenin- and VE-cadherin-containing complexes, as shown by a significant decreased co-immunoprecipitation between them upon CCM1 silencing (Fig. 2D). The level of remaining complex was consistent with the remaining level of CCM1 (Fig. 2A), suggesting that CCM1 acted as a scaffold for ROCK2 at VE-cadherin complexes. We indeed showed that CCM1 interacted with ROCK2 as well as with ROCK1 (Fig. 2E).

As both CCM1 and ROCK2 loss lead to increased stress fiber production (Fig. 1), we wondered whether ROCK1 would be overactivated in these conditions. For this purpose, we measured ROCK1 and ROCK2 kinase activity by adapting an *in vitro* kinase assay from that published by Rubenstein et al. (Rubenstein et al., 2007). ROCK1 or ROCK2 were specifically immunoprecipitated from confluent HUVECs that had been silenced or not for CCM1. Their intrinsic ability to phosphorylate the GST–MYPT (654-880) fragment as a substrate was assayed. We found that CCM1 depletion had no effect on ROCK2 intrinsic kinase activity but instead increased ROCK1 intrinsic activity (Fig. 2F). Since the ROCK1 protein level was unchanged (Fig. 2A), these data indicate that the total kinase activity of ROCK1 increased upon CCM1 depletion. Remarkably, ROCK2 depletion led to an increase in ROCK1 kinase activity that was similar to that observed upon CCM1 depletion (Fig. 2F). Consistent with this, the increased kinase activity upon loss of CCM1 or ROCK2 correlated with an increase in the level of ROCK1 phosphorylation at Ser1333 (Fig. 2G), an indicator of ROCK1 activation (Chuang et al., 2013).

Taken together, these results suggest that the CCM complex, by recruiting ROCK2 to VE-cadherin complexes and inhibiting ROCK1, allows the assembly of a competent actin cytoskeleton to maintain the homeostasis between cell–cell and cell–ECM adhesion. In addition, these data pinpoint ROCK1 as the likely Rho kinase responsible for the increased contractility of CCM1- and CCM2-depleted HUVECs.

Silencing of ROCK1 restores cortical actin and cell–cell junction integrity *in vitro* and *in vivo*

To directly address whether ROCK1 overactivation is responsible for the increased contractility in CCM-depleted HUVECs, we tested whether the *CCM* mutant phenotype could be rescued by ROCK1 depletion. Strikingly, upon additional silencing of ROCK1, sparsely plated CCM1- or CCM2-depleted HUVECs showed normal cobblestone shapes supported by a cortical actomyosin cytoskeleton (Fig. 3A,B; Fig. S3A,B). The percentage of cells bearing transversal stress fibers was restored to the level of the control (Fig. 3C; Fig. S3C). By contrast, additional silencing of ROCK2 did not restore a normal morphological phenotype; cells remained elongated with transversal actin stress fibers (Fig. 3A–C; Fig. S3B,C). Monolayers of double-transfected HUVECs were morphologically indistinguishable from control HUVECs (Fig. 3A; Fig. S3A). Both the morphology and thickness of VE-cadherin junctions were restored after ROCK1 deletion in CCM1- or CCM2-silenced HUVECs (Fig. 3D,E; Fig. S3D,E) or hCMEC/D3 cells (Fig. S3F,G). By contrast, additional ROCK2 depletion worsened the phenotype, perturbing cell–cell junctions to the point of visible ruptures between cells, demonstrating the unique role of ROCK1 in increasing stress fiber-dependent cell contractility (Fig. 3D,E; Fig. S3D–G).

To test whether overactivation of Rock1 has a relevant role *in vivo*, we analyzed the endothelial actin phenotype of *ccm1* mutant zebrafish embryos. We used two independent antisense oligonucleotide morpholinos (MO1 and MO2) (Fig. S5A) against the sole homolog of *rock1* present in the zebrafish genome (Chu et al., 2012) and verified their knockdown efficacy by western blotting (Fig. S5B). Next, we injected MO1 or MO2 into *krit1*/*ccm1*^{ty219c} mutants and characterized the actin phenotype of endothelial cells of the common cardinal vein at 48 h post fertilization (hpf) (Fig. 3F). Whereas WT common cardinal vein cells displayed a strong cortical actin belt, in *krit1*/*ccm1*^{ty219c} mutants these cells had significantly increased numbers of transversal actin stress fibers as indicated by a reduction in the ratio of cortical versus intracellular pools of actin (Fig. 3F, quantified in G). Consistent with our *in vitro* findings in HUVECs, knockdown of zebrafish Rock1 in *krit1*/*ccm1*^{ty219c} mutants significantly increased the ratio of cortical versus intracellular actin pools and reduced stress fiber formation to WT levels (Fig. 3F,G). Hence, as *in vitro*, zebrafish Rock1 exerts a critical role for controlling the distribution of cellular actin and stress fiber formation upon loss of CCM1.

To check whether the rescue of endothelial cell morphology upon additional ROCK1 silencing is accompanied with a restoration of the endothelial barrier function, the electrical barrier resistance of confluent monolayers was measured by quantifying the impedance of HUVECs. Consistent with previous findings (Whitehead et al., 2009), depletion of CCM1 or CCM2 decreased the impedance plateau, a result that argues in favor of a reduced permeability barrier

Journal of Cell Science (2018) 131, jcs216093. doi:10.1242/jcs.216093

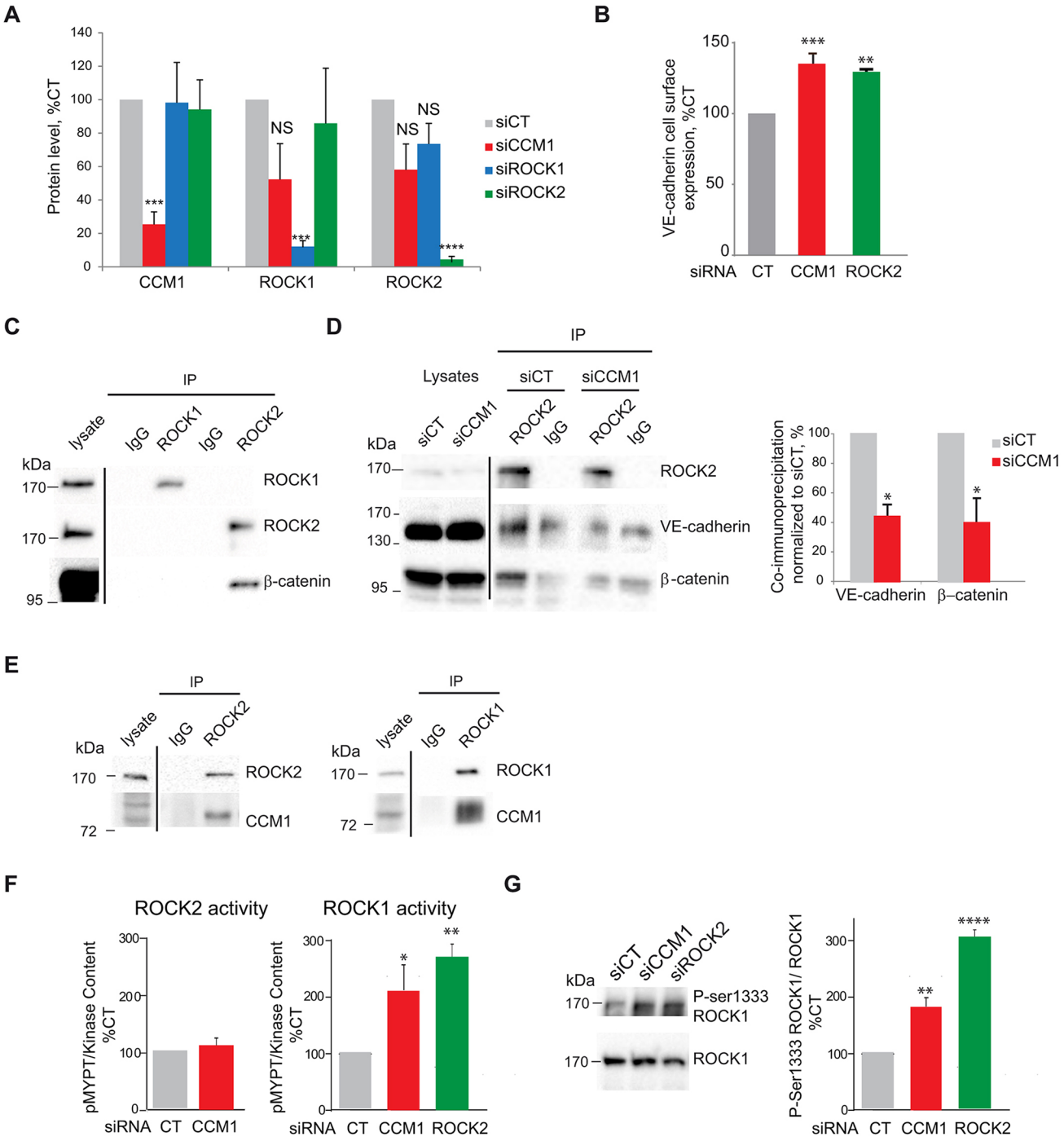

Fig. 2. CCM1 is a scaffold controlling ROCK1 and ROCK2. (A) Bar graphs representing the level of CCM1, ROCK1 and ROCK2 proteins in silenced HUVECs. Error bars, s.e.m. (n=5). (B) Bar graph representing the VE-cadherin cell surface level as measured by flow cytometry. Error bars, s.e.m. (n=4). (C) Immunoprecipitations (IP) of endogenous ROCK1 and ROCK2 from confluent HUVECs showing specific co-immunoprecipitation of β-catenin with ROCK2 but not ROCK1. (D) Western blot showing that CCM1 depletion prevents β-catenin and VE-cadherin co-immunoprecipitation with ROCK2 (left). Right, quantification of the relative percentage of co-immunoprecipitated β-catenin or VE-cadherin with immunoprecipitated ROCK2. Error bars, s.e.m. (n=3). (E) Co-immunoprecipitation of CCM1 with ROCK2 (left) or ROCK1 (right) from confluent HUVECs. These western blots are representative of more than three experiments. (F) Left, ROCK2 intrinsic kinase activity upon CCM1 depletion. Error bars, s.e.m. (n=4). Right, ROCK1 intrinsic kinase activity upon CCM1 or ROCK2 depletion. Error bars, s.e.m. (n=5 for siCCM1 and 3 for siROCK2). (G) Left, western blot of ROCK1 phosphorylated at Ser1333 (P-ser1333 ROCK1) and ROCK1. Right, quantification of the relative percentage of P-ser1333 ROCK1 to ROCK1. Error bars, s.e.m. (n=4). *P<0.05, **P<0.005; ****P<0.0001; NS, not significant (one-way ANOVA with Tukey's multiple comparisons). Vertical bars on western blots indicate irrelevant cropped lanes. CT, control.

(Fig. 4A,B; Fig. S4A,B). Additional ROCK1 silencing in CCM1- or CCM2-depleted monolayers restored the impedance to its normal plateau value as compared with control or siROCK1 monolayers (Fig. 4A,B; Fig. S4A,B). By contrast, depletion of ROCK2 led to a dramatic drop in the impedance when depleted alone or in combination with CCM1 (Fig. 4A). The inability of these cells to

Journal of Cell Science (2018) 131, jcs216093. doi:10.1242/jcs.216093

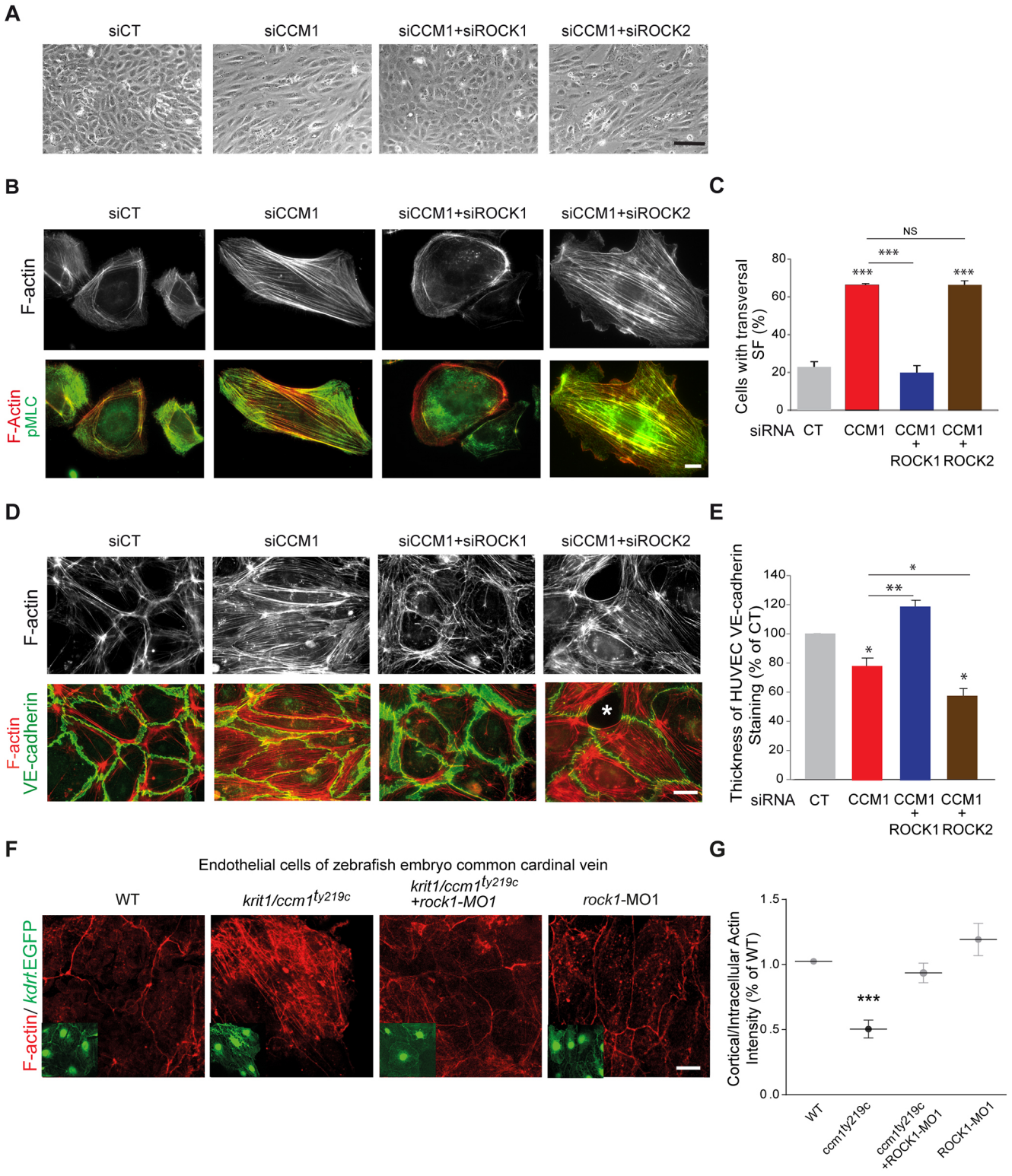

Fig. 3. See next page for legend.

form competent cell–cell junctions led to their detachment from the substrate preventing any quantification of the permeability barrier in these serum-deprived conditions.

We next assayed the effect of ROCK1 overactivation on the contractile forces exerted at cell–cell junctions in CCM1- or CCM2-depleted HUVECs. Tensile forces at cell–cell junctions were measured by means of traction force microscopy on cell doublets spread on FN-coated 5 kPa polyacrylamide gels. Whereas depletion of CCM proteins led to an increase of cell–cell forces by 1.6-fold for CCM1 (Fig. 4C) and 2.3-fold for CCM2 (Fig. S4C), ROCK1 depletion alone showed a tendency for lowering cell–cell forces (Fig. 4C). Consistent with their normal cell–cell junction

Journal of Cell Science (2018) 131, jcs216093. doi:10.1242/jcs.216093

Fig. 3. ROCK1 silencing restores normal adhesive and contractile phenotypes in CCM1-depleted HUVECs and zebrafish *ccm1* mutant CCV endothelial cells. (A) Representative phase contrast images of siRNA-transfected HUVEC monolayers. (B) Representative immunofluorescence of sparsely plated siRNA-transfected HUVECs stained for F-actin (gray) and merged images with pMLC. (C) Percentage of cells with transversal actin stress fibers. Error bars, s.e.m. (n=4 except for CCM1+ROCK2 and CCM2 +ROCK2 where n=2). (D) Representative immunofluorescence of F-actin (gray) and merged images with VE-cadherin of HUVEC monolayers on 20 µg/ml FN-coated coverslips at 72 h post plating. The asterisk indicates the zone of detachment for intercellular junctions. (E) Quantifications of VE-cadherin thickness from immunofluorescence staining of HUVECs presented as a percentage of control. The CT and CCM1 data are also shown in Fig. 1I. Error bars, s.e.m. (n=4 except for CCM1+ROCK1 where n=3 and CCM1+ROCK2 where n=2). In C and E, *P<0.05, **P<0.005, ***P<0.0005; NS, not significant (one-way ANOVA with Dunett's multiple comparisons). (F) Representative immunofluorescence of F-actin staining and Tg(*kdrl:* EGFP)-labeled endothelial cells (insets) of the CCV. (G) Quantification dot plot with s.e.m. of the intensity ratios of peripheral cortical actin over intercellular actin in WT (n=13), *krit1*/*ccm1*^{ty219c} (16 embryos, 42 cells), *krit1*/*ccm1*^{ty219c}+*rock1*-MO (16 embryos, 47 cells), and WT+*rock1*-MO (12 embryos, 26 cells) CCV regions; results were normalized to the WT ratio and the experiment was performed three times on independent zebrafish cohorts. ***P<0.005 (one-way ANOVA with Tukey's multiple comparisons post-test). Scale bars: 50 µm (A) 10 µm (B,D,F). CT, control.

morphology and permeability, the additional depletion of ROCK1 in CCM1- or CCM2-depleted cells restored low cell–cell forces (Fig. 4C; Fig. S4C). These results suggest that, in the context of CCM1- or CCM2-depleted cells, overactivation of ROCK1 modified the actin cytoskeleton leading to excessive pulling traction forces at cell–cell junctions and disrupting the endothelial integrity.

In conclusion, the depletion of ROCK1 in CCM1- or CCM2-depleted cells or *ccm1* mutant zebrafish embryos is sufficient to restore a honeycomb-shaped contractile network with normalized cell–cell forces allowing for the reestablishment of endothelial integrity.

Silencing of ROCK1 rescues the heart morphogenesis defects in *ccm1* mutant zebrafish embryos

Since knockdown of Rock1 in zebrafish *krit1*/*ccm1*^{ty219c} mutant embryos restores normal endothelial cell morphology, we wondered whether it would also rescue their heart morphogenesis defects. Indeed, loss of Ccm1 in zebrafish causes cardiac ballooning, heart looping defects and a failure in the formation of endocardial cushions (Hogan et al., 2008; Mably et al., 2006). Compared to WT (Fig. 5A; Fig. S5C), *krit1*/*ccm1*^{ty219c} mutant embryos exhibited a profound cardiac phenotype characterized by ballooning defects and a lack of formation of cardiac cushions (Fig. 5B; Fig. S5D,D′). This later phenotype was mainly due to a failure of endocardial cells at the atrioventricular border to acquire a cuboidal shape (Fig. 5B′ as compared to Fig. 5A′ and Fig. S5C′). Knockdown of Rock1 in WT embryos did not affect the formation of the atrioventricular canal or of cardiac cushions (Fig. 5D,D′; Fig. S5E,E′). Strikingly,

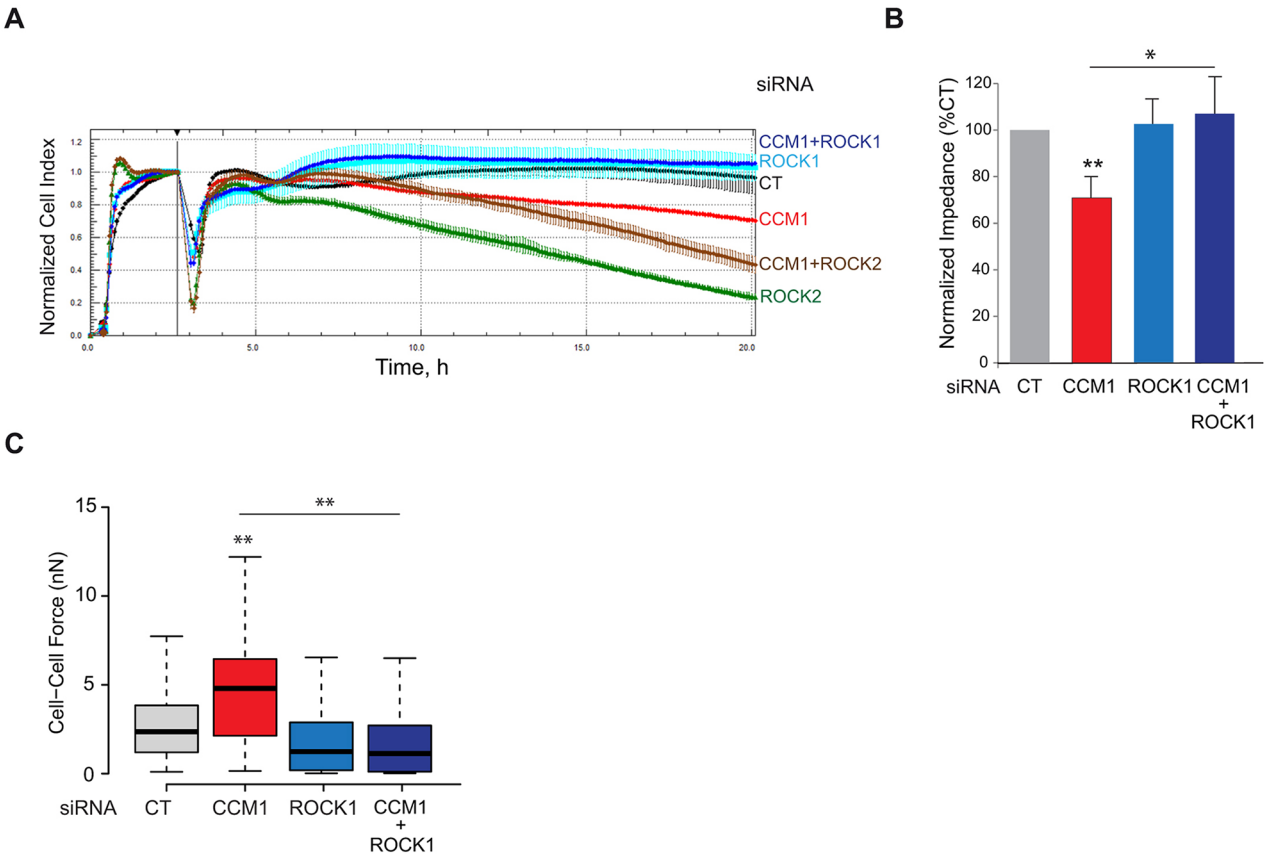

Fig. 4. ROCK1 silencing restores the functional permeability barrier in CCM1-depleted HUVECs and intercellular tensile forces. (A) Representative kinetics of the impedance of silenced HUVEC monolayers. Cell indexes were normalized at the serum starvation time (vertical line). (B) Bar graph quantification of the plateau value of normalized impedance after 25 h. Error bars, s.e.m. (n=6). (C) Cell–cell forces measurement from traction force microscopy of HUVEC doublets plated on top of 5 kPa FN-coated polyacrylamide gel. Between 45 and 80 doublets were analyzed (n=4). The box represents the 25–75th percentiles, and the median is indicated. The whiskers show the s.e.m. *P<0.05; **P<0001 (one-way ANOVA with Dunnett's multiple comparisons test). CT, control.

Journal of Cell Science (2018) 131, jcs216093. doi:10.1242/jcs.216093

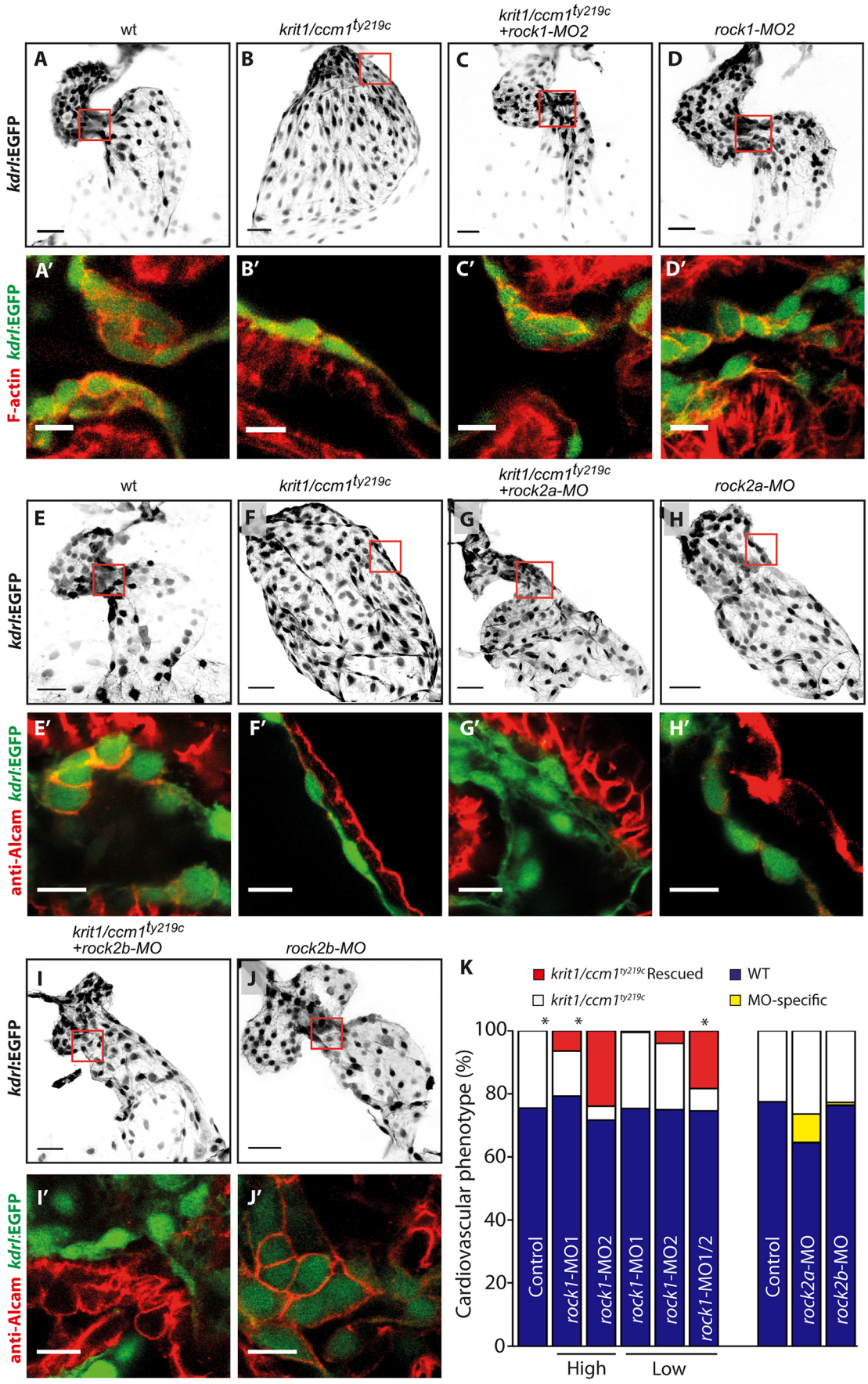

Fig. 5. See next page for legend.

Journal of Cell Science (2018) 131, jcs216093. doi:10.1242/jcs.216093

Fig. 5. ROCK1 silencing in *ccm1* zebrafish mutant embryos rescues cardiac morphogenesis. (A–J) Endocardial cells, marked by Tg(*kdrl*:EGFP) (inverted images) at 48 hpf. Details with single confocal plane section of the atrioventricular canal (AVC) are shown in A′–J′. Scale bars: 30 µm (main images); 10 µm (detailed images). (K) Quantification of the number of embryos that showed a phenotypic rescue of the *krit1*/*ccm1*^{ty219c} cardiac phenotype at 48 hpf. Embryos from *krit1*/*ccm1*$^{ty219c/+}$ incrosses were 75% phenotypically WT (blue bars), while 25% showed *krit1*/*ccm1*^{ty219c} mutant phenotype of cardiac ballooning (white bars). Embryos from *krit1*/*ccm1*$^{ty219c/+}$ incrosses that were injected with high doses of *rock1*-MO1 and -MO2 showed a rescue of the cardiac ballooning (red), whereas embryos injected with low MO doses failed to show significant numbers with rescue. However, when combined, low doses of *rock1*-MO1 and -MO2 rescued the cardiac ballooning phenotype in *krit1*/*ccm1*^{ty219c} mutant embryos as efficiently as single high dose MOs. Total numbers quantified, from a set of three independent zebrafish cohorts, are *n*=195 for control embryos; *rock1*-MO1 injected at high dose, *n*=232; *rock1*-MO2 at high dose, *n*=126; *rock1*-MO1 at low dose, *n*=167; *rock1*-MO2 at low dose, *n*=148; and combined *rock1*-MO1 and MO2 at low dose, *n*=134. **P*<0.05 (two-way ANOVA with Dunett's multiple comparisons post-test). Embryos from *krit1*/*ccm1*$^{ty219c/+}$ incrosses that were injected with either *rock2a*-MO1 or *rock2b*-MO2 did not rescue the cardiac ballooning phenotype, however, a fraction of the sibling population show MO-specific defects that are similar to the *krit1*/*ccm1*^{ty219c} phenotype. Control for *rock2a*-MO, *n*=230; *rock2a*-MO, *n*=265; control for *rock2b*-MO, *n*=526; *rock2b*-MO, *n*=317.

endocardial cells regained a cuboidal shape at the atrioventricular canal upon *rock1* MO injection into *krit1*/*ccm1*^{ty219c} mutants (Fig. 5C′; Fig. S5F′,H′). This was accompanied by the restoration of the ventricular chamber morphology (Fig. 5C; Fig. S5F,H) compared to the WT condition (Fig. 5E,K; Fig. S5C). Despite the rescue of most of the cardiac morphology, the atrium was still abnormally dilated. To examine putative off-target effects of MO1 or MO2, we used each morpholino at lower doses at which no cardiac rescue was achieved (Fig. 5K; Fig. S5I–L′). When co-injected, these low doses of each MO were sufficient to cause the cardiac rescue phenotype in *krit1*/*ccm1*^{ty219c} mutants (Fig. 5J,K; Fig. S5M–N′) suggesting specificity of each MO.

To further corroborate our *in vitro* data, we asked whether knockdown of Rock2 phenocopies the cardiac ballooning defects of *krit1*/*ccm1*^{ty291c} mutants. In zebrafish, two genes, *rock2a* and *rock2b*, encode for Rock2 proteins. Phylogenetic protein sequence analysis with ROCK2 proteins from different species reveal that zebrafish Rock2a has a greater similarity to human ROCK2 (76%), whereas zebrafish Rock2b is more divergent (66%) (Fig. S6A,B). We therefore assumed divergent roles for Rock2a and Rock2b and used independent antisense morpholinos against the two zebrafish *rock2* genes (Fig. S6C) to analyze cardiac phenotypes in Rock2a- or Rock2b-depleted *krit1*/*ccm1*^{ty219c} mutants. Their knockdown efficacy was verified by western blotting (Fig. S6D).

In agreement with our *in vitro* data, we did not observe a rescue of chamber morphogenesis or restoration of cardiac cushions in *rock2a*-MO- or *rock2b*-MO-injected *krit1*/*ccm1*^{ty219c} mutants (Fig. 5D,J). Knockdown of Rock2a in *krit1*/*ccm1*^{ty219c} mutants led to smaller, condensed ventricles and dilated atria (Fig. 5G). However, cushion formation remained impaired, as evidenced by the lack of staining of the endothelial marker Alcam in endocardial AVC cells (Fig. 5G′). We confirmed that *krit1*/*ccm1*^{ty219c} mutants were not rescued by genotyping all WT embryos. Instead, we found that, among embryos that appeared phenotypically like *krit1*/*ccm1*^{ty219c} mutants, as characterized by dilated heart chambers and formation of pericardial edemas, ∼25% were genetically WT embryos (Fig. 5K, yellow bars). Further analysis revealed that depletion of Rock2a in these WT embryos led to an impaired chamber morphogenesis and a loss of AVC formation with loss of cuboidal cell shape and reduced Alcam staining (Fig. 5H,H′,K). This phenotype is specific to the knockdown of Rock2a and is reminiscent of the *krit1*/*ccm1*^{ty219c} mutant phenotype.

Knockdown of Rock2b causes laterality defects leading to reversed or bilaterally oriented hearts (Fig. 5E,J), as previously reported (Wang et al., 2011). However, cardiac cushion formation in Rock2b-depleted hearts was not affected in either WT or *krit1*/*ccm1*^{ty219c} mutants, which was characterized by strong Alcam staining in WT and lack thereof in *krit1*/*ccm1*^{ty219c} mutants (Fig. 5I′,J′). These results point at a diversification in function of Rock2a and Rock2b during zebrafish cardiac development, with Rock2a maintaining the conserved function of ROCK2 protein in the CCM pathway.

Taken together, these *in vivo* results not only reinforce our model that ROCK1 overactivation is a critical contributor mediating actin cytoskeleton defects but directly identifies ROCK1 as a central player in the *ccm1* mutant heart morphogenesis defect *in vivo*. Further, partial rescue of the cardiac phenotype in MO-driven ROCK1 zebrafish *in vivo* suggests that both endothelial and cardiac tissue integrity necessitate robust regulation of ROCK1 kinase activity.

DISCUSSION

Upregulation of RhoA/ROCK-dependent contractility and the ensuing loss of endothelial barrier function is a hallmark of CCM pathology. Previous studies have shown that the CCM1–CCM2 complex regulates cell contractility by controlling RhoA activation (Borikova et al., 2010; Stockton et al., 2010; Whitehead et al., 2009) or stability (Crose et al., 2009). Our work reveals that the CCM1–CCM2 complex acts as a scaffold controlling complementary functions of ROCK1 and ROCK2 to organize the contractile actomyosin cytoskeleton at cell–ECM and cell–cell adhesions, thereby maintaining endothelial integrity and ensuring heart morphogenesis in zebrafish embryos.

ROCK1 and ROCK2 are both required to organize the actomyosin cytoskeleton at AJs and FAs

Following the work of Yoneda and colleagues (Yoneda et al., 2005), several studies have shown that ROCK1 and ROCK2 bear distinct but complementary functions on actomyosin cytoskeleton organization, cell migration and polarity (Lock and Hotchin, 2009; Newell-Litwa et al., 2015). However to our knowledge, our work is the first to demonstrate that they have complementary functions in the contractile and adhesive homeostasis at AJs and FAs in endothelial cell monolayers. ROCK1 activity favors the assembly of ventral actin stress fibers and cell–ECM adhesions, while ROCK2 activity is necessary for VE-cadherin-dependent cell–cell adhesion by promoting the assembly of a cortical actin rim. This agrees with the known association of ROCK1 with FN-bound adhesion complexes (Robertson et al., 2015) and its ability to regulate integrin-anchored actin stress fibers for the cell to adopt a front-to-back polarity (Lock and Hotchin, 2009; Newell-Litwa et al., 2015; Yoneda et al., 2005) and with ROCK2 localization at the periphery of cells (Yoneda et al., 2005), likely through interaction of its PH domain with phosphoinositides (Tumusiime et al., 2009). Furthermore, in endothelial cells, ROCK2 is recruited at VE-cadherin complexes in AJs where it is involved in AJ maturation in order to maintain cell–cell cohesion during sprouting angiogenesis (Wimmer et al., 2012).

We demonstrate that both ROCKs are required for the correct organization of the cortical actin arcs and ventral actin stress fibers. It has been shown that cortical arcs assemble from small α-actinin-crosslinked F-actin bundles derived from Arp2/3-nucleated

Journal of Cell Science (2018) 131, jcs216093. doi:10.1242/jcs.216093

lamellipodial actin filament network (Hotulainen and Lappalainen, 2006). The contraction of these actin arcs converts the dorsal stress fibers into ventral actin stress fibers connected on both sides to a FA (Burnette et al., 2014; Burridge and Wittchen, 2013; Hotulainen and Lappalainen, 2006). Our results suggest that ROCK2 is necessary for the polymerization of the cortical actin arcs. We observed that its loss leads to the appearance of α-actinin-crosslinked F-actin patches in dorsal ruffles accompanied with a decrease in cortical actin filaments. Interestingly, Newell-Litwa et al. have shown that ROCK2 specifically inhibits Rac activation and phosphorylates cofilin (Newell-Litwa et al., 2015). A relief of Rac1 and cofilin inhibitions upon ROCK2 loss may explain the accumulation of Arp2/3-dependent α-actinin-crosslinked actin bundles whose elongation would be limited by the severing activity of cofilin. In a complementary way, ROCK1 seems to be involved in the contractility of the cortical actomyosin arcs and the subsequent formation of ventral stress fibers. Indeed, its loss leads to a less-compact cortical actin rim and low cell–cell tension, while its overactivation upon ROCK2 loss generates more ventral stress fibers and increased cell–cell tension. This is in good agreement with its higher capacity than ROCK2 to phosphorylate myosin II light chain (Newell-Litwa et al., 2015; Yoneda et al., 2005) and its reported role on junctional tension in epithelial cells (Priya et al., 2017).

The CCM1–CCM2 complex orchestrates ROCK1 and ROCK2 functions to preserve the endothelial mechanical homeostasis

A regulatory link between ROCK1 and ROCK2 has never been investigated so far in endothelial cells. Contrary to the trivial model of the strict spatial segregation of ROCK1 at FAs and ROCK2 at AJs, it has been shown that the two isoforms expressed as GFP fusions display similar localization to actin-rich compartments (Newell-Litwa et al., 2015). In support of these results, *in vivo* localization studies in mouse tissues utilizing immunofluorescence and electron microscopy previously revealed the presence of ROCK1 and ROCK2 at AJs and on actin stress fibers (Iizuka et al., 2012).

Lack of specific antibodies to immunostain the human ROCKs preclude their localization in HUVECs as also reported in other human cells (Vega et al., 2011). However, based on our results from immunoprecipitation assays, we propose that the CCM complex orchestrates ROCK1 and ROCK2 functions by controlling their molecular environment and by safe-guarding the cell against an excess of ROCK1 activity. Mechanistically, we showed that the CCM1–CCM2 complex serves as a scaffold promoting the interaction of ROCK2 with VE-cadherin–β-catenin complexes and the inhibition of ROCK1 kinase activity (Fig. 6). ROCK2 has previously been shown to be directed to the AJs by Raf-1 (Wimmer et al., 2012). Like Raf-1, CCM1 is a Rap1 effector (Béraud-Dufour et al., 2007) whose recruitment at VE-cadherin complexes depends on its interaction with Rap1 (Glading et al., 2007). A large complex comprising Rap1, Raf-1 and CCM1 may be necessary to recruit ROCK2 at VE-cadherin complexes. As both loss of ROCK2 and the CCM1–CCM2 complex result in increased ROCK1 catalytic activity, one can hypothesize that the CCM complex would enable ROCK1 inhibition by ROCK2. Phosphorylation of ROCK1 at Ser1333 has been shown to correlate with its activation (Chuang et al., 2013), likely by opening its closed conformation to expose its

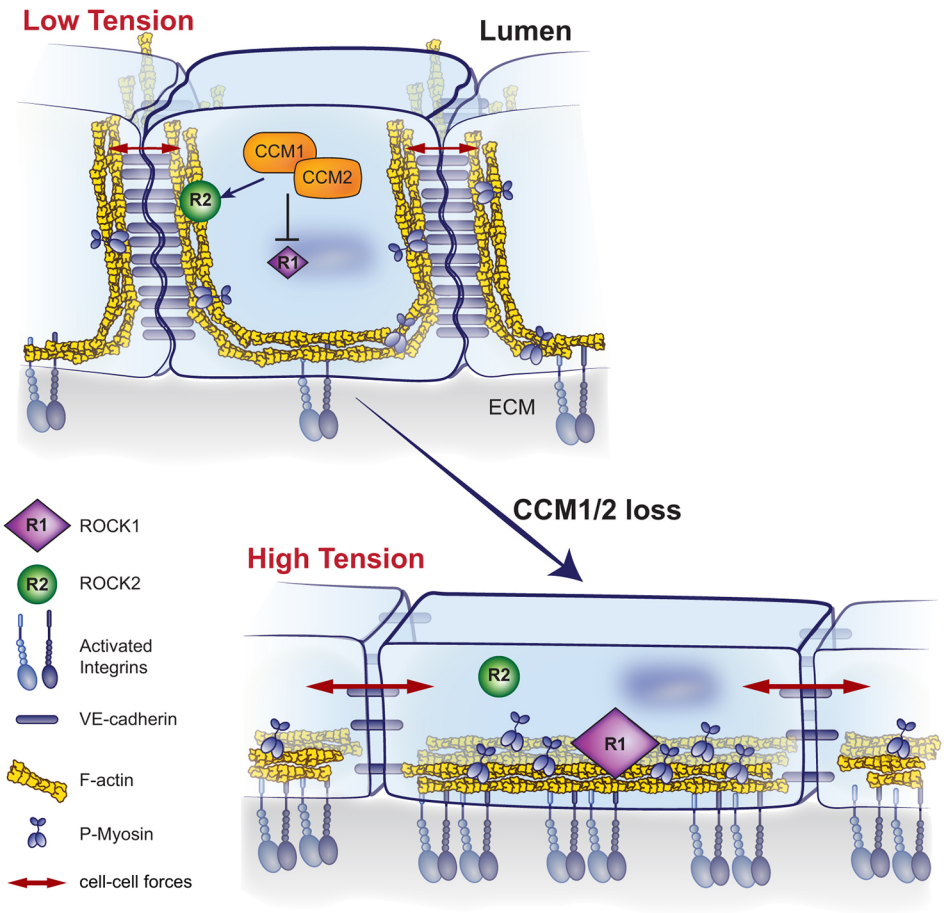

Fig. 6. Model of the CCM-dependent control of ROCK1 and ROCK2 functions to preserve endothelial mechanical integrity. The CCM1–CCM2 complex orchestrates ROCK1 and ROCK2 functions to maintain the adhesive and contractile endothelial homeostasis by acting as a scaffold for ROCK2 at AJ and by limiting the kinase activity of ROCK1. Overactivated ROCK1 upon loss of the CCM1–CCM2 complex stimulates actin stress fibers and focal adhesions formation resulting in higher intercellular forces and, ultimately, destabilizing intercellular junctions.

Journal of Cell Science (2018) 131, jcs216093. doi:10.1242/jcs.216093

kinase domain. In a preliminary proteomic analysis, we identified a protein phosphatase that associates with both ROCK1 and ROCK2 in a CCM1-dependent manner (data not shown). Increased phosphorylation of ROCK1 at Ser1333 upon CCM1 or ROCK2 loss suggests that, in presence of the CCM complex and ROCK2, the activity this protein phosphatase may limit the level of phosphorylation of ROCK1. Additional studies will be required to unravel the complex mechanism finely tuning the activation of ROCK1.

Junctional RhoA and Rac are antagonistically activated but together have essential functions for AJ integrity (Yamada and Nelson, 2007). Interestingly, CCM2 is a scaffold for Rac and RhoA (Uhlik et al., 2003; Whitehead et al., 2009) and limits RhoA activation (Borikova et al., 2010; Stockton et al., 2010; Whitehead et al., 2009). Here, we show that CCM1 acts as a scaffold promoting the interaction of ROCK2 with VE-cadherin–β-catenin complexes and limiting ROCK1 activity. We propose that the coordination between ROCK1 and ROCK2, besides from regulating actin-binding partners involved in maintenance of cell–cell junctions, could also be involved in the fine spatio-temporal regulation of RhoA and Rac activities. It has been shown that ROCK1 maintains a constant level of active RhoA at zonula adherens in epithelial cells by preventing the cortical recruitment of p190RhoGAP (also known as ARHGAP5) (Priya et al., 2015). Therefore, overactivation of ROCK1 at cell–cell junctions in CCM1- or CCM2-depleted endothelial cells may lead to an abnormally high level of active RhoA and subsequently to a lower level of active Rac because they exert a negative regulatory effect on each other (Sander et al., 1999). However, Rac stabilizes VE-cadherin trans-dimers in AJs by counteracting actomyosin tension (Daneshjou et al., 2015). Reduced Rac activation upon ROCK1 overactivation could explain the destabilizing effect of ROCK2 depletion on AJ.

We showed that the control of ROCKs by CCM1–CCM2 complex is a key mechanism for preserving endothelial cell mechanics and barrier function. Assembly of adhesion sites between neighboring cells and with the ECM are two interconnected processes that depend on the generation of local forces. The restoration of normal levels of forces and functional cell–cell junctions upon additional depletion of ROCK1 supports the conclusion that overactivated ROCK1 generates excessive traction forces on cell–cell junctions either at distance or/and locally in CCM1- or CCM2-depleted cells. Shear stress is a specific mechanical signal that endothelial cells experience. We have already shown that the CCM1–CCM2 complex is required for a correct morphological response of endothelial cells to shear stress (Jilkova et al., 2014). By controlling ROCK1 and ROCK2 activities, the CCM complex may potentially function as a molecular integrator to finely tune the endothelial cell response to a complex array of mechanical inputs coming from shear stress and wall stiffness.

ROCK1 is a therapeutic target of choice for CCM disease

We have shown that downregulation of ROCK1, but not ROCK2, is crucial to restore a normal junctional phenotype and endothelial barrier function in CCM-depleted endothelial cells. Moreover, our *in vivo* experiments demonstrate that ROCK1 overactivation crucially contributes to the *ccm1* heart phenotype in zebrafish embryos. As a major result, we showed that ROCK1 silencing restored the cuboidal shape of *ccm1* mutant endocardial cells as well as the formation of the cardiac cushions and of the ventricular chamber. It is likely that knockdown of ROCK1 allowed the endocardial layer to regain its capacity to undergo morphogenetic changes. Strikingly, knockdown of Rock2a did not rescue *ccm1* mutant heart defects and provoked defects reminiscent of those observed upon CCM1 loss in the WT background. In consequence, the use of ROCK1-targeted drugs, instead of the current broad ROCK inhibitors, could likely be highly beneficial and clinically efficacious by limiting the side-effect of also inhibiting ROCK2. ROCK1-specific inhibitors may allow a longer-term treatment than current broad ROCKs inhibitors which, while having shown their efficacy on lowering the number of lesions and the associated hemorrhages in mouse models of CCM disease (McDonald et al., 2012; Shenkar et al., 2017), cannot be administrated for long periods to patients.

MATERIALS AND METHODS

Reagents and antibodies

Bovine plasma fibronectin (FN) was purified from bovine plasma by affinity chromatography (Albiges-Rizo et al., 1995). Rat tail collagen I was from Corning (ref. 354236). Human recombinant vitronectin (VN) was from Sigma (ref. SRP3186-250UG). EBM medium and growth factors (bullet kit) were from Lonza. Table S1 lists the commercial antibodies used. Polyclonal rabbit anti-CCM1 was raised against a recombinant CCM1 fragment comprising amino acids 1–400, produced in *Escherichia coli* and affinity purified, and used for western blotting at 1:1000 (Faurobert et al., 2013). VE-cadherin–rabbit anti-human pAb was kindly provided by Dr Danielle Gulino (iRTSV/BCI Dept, CEA, France) and used for immunofluorescence at 1:1000. Antibody against ROCK1 phosphorylated at Ser1333 was produced in rabbit and affinity purified (Chuang et al., 2013). Agarose–protein-G beads were purchased from Roche (ref. 1171941600), Dynabeads protein G from Life Technologies (ref. 10003D) and recombinant GST-fused MYPT protein was from Millipore (ref. 12-457).

Cell culture and transfections

Pooled HUVECs were obtained from Lonza and grown in complete EGM-2 medium supplemented with 100 U/ml penicillin and 100 µg/ml streptomycin at 37°C in a 5% CO_2 and humidified chamber according to the manufacturer's instructions. HUVECs (1.5×10^6 cells) were transfected twice at 24 h intervals with 20 nM siRNA and 45 µl Lipofectamine RNAi max (Life Technologies, ref. 13778-150) according to the manufacturer's instructions. For double transfections, 20 nM of each siRNA was used with 45 µl Lipofectamine RNAi max. siRNA duplexes for control (5′-AGGUAGUGUAAUCGCCUUG-3′) were synthetized by Eurogentec. Other siRNAs targeted: CCM1 (Ambion cat. no. AM16704; lot no. ASO0Y8C5), CCM2 (Dharmacon smartpool ON-TARGET plus Thermo Scientific ref. L-014728-01), ROCK1 (Dharmacon smartpool ON-TARGET plus Thermo Scientific ref. L-003536-00; Dharmacon individual ON-TARGET plus Thermo Scientific ref. J-003536-06 and J-003536-08), ROCK2 (Dharmacon smartpool ON-TARGET plus Thermo Scientific ref. L-004610-00; Dharmacon individual ON-TARGET plus Thermo Scientific ref. L-004610-06 and L-004610-08) and β1 integrin (Dharmacon smartpool SMARTpool: siGENOME ITGB1 ref M-004506-00). hCMEC/D3 cells were grown as previously described (Weksler et al., 2005) and transfected as above.

Immunoprecipitation

Confluent HUVECs were washed once with PBS, lysed in lysis buffer (20 mM Tris-HCl pH 7,4, 150 mM NaCl, 10% glycerol, 1% Triton X-100, 2 mM $CaCl_2$, 50 mM Na_2MoO_4•$2H_2O$, 1 mM DTT, 20 mM NaF, 20 mM β-glycerophosphate, 1 mM Na_3VO_4, proteases inhibitor cocktail) on ice. The lysate was centrifuged at 4°C for 15 min at 15,000 ***g***. The supernatant was pre-cleared for 1 h at 4°C with agarose–protein G beads or dynabeads coupled to protein G. Meanwhile, agarose–protein G beads or dynabeads coupled to protein G were saturated with 3% BSA solution in PBS for 30 min and then incubated with antibody (anti-ROCK1, anti-ROCK2 or IgG control antibody) for 1 h at 4°C. Precleared lysate was incubated with pre-coupled beads overnight at 4°C. Beads were then washed three times with supplemented with 200 mM Nacl, then three times lysis buffer and finally three times in lysis buffer supplemented with 50 mM NaCl. Beads

were resuspended with 1× Laemmli buffer and boiled at 95°C for 5 min before western blot analysis.

In vitro kinase activity assay

Confluent transfected HUVECs were washed once with PBS, lysed in lysis buffer (50 mM Tris-HCl pH 7,4, 150 mM NaCl, 5% glycerol, 1% Triton X-100, 10 mM $MgCl_2$, 1 mM DTT, 20 mM NaF, 20 mM β-glycerophosphate, 1 mM Na_3VO_4, proteases inhibitor cocktail) on ice. The lysate was centrifuged at 4°C for 15 min at 15,000 ***g***. The supernatant was pre-cleared for 15 min with protein G dynabeads. Protein G dynabeads were incubated with antibody (anti-ROCK1 K18 or anti-ROCK2 C20 antibodies, both Santa Cruz Biotechnology) for 1 h at 4°C. Pre-cleared lysate was incubated with pre-coupled beads for another 1 h at 4°C. Afterwards, beads were washed with lysis buffer and a half of the solution was taken for quantification of precipitated ROCK by western blotting, and the other half was suspended in kinase buffer (lysis buffer+10 µM ATP) for further *in vitro* kinase activity assay. Different dilutions (50%, 25%, 6.25%) of beads were then mixed with 1 µg of recombinant substrate MYPT with or without the ROCK inhibitor Y-27 632 (Sigma Aldrich) as an internal control of ROCK specific phosphorylation, and incubated for 30 min at 30°C on a shaker. Enzymatic reaction was stopped by adding Laemmli buffer and boiled at 95°C for 10 min. Samples were subjected to western blotting using anti-pMYPT1 (Thr696) antibody from Millipore. The intrinsic kinase activity for each sample was calculated as the level of phosphorylated MYPT normalized to the quantity of immunoprecipitated kinase.

Western blot analysis

Cells were lysed in Laemmli buffer, protein extract from whole zebrafish embryos was lysed in RIPA buffer. Equal amount of proteins were loaded on gel and separated on SDS-PAGE, and transferred on PVDF membranes. Immunological detection was achieved with horseradish peroxidase (HRP)-conjugated secondary antibody. Peroxidase activity was visualized with clarity western ECL substrate (Bio-Rad Laboratories) using a ChemiDoc MP imaging system (Bio-Rad Laboratories). Densitometric quantification of the bands was performed using the Image Laboratory program (Bio-Rad Laboratories).

Quantitative RT-PCR

Total RNA was extracted from cells using the NucleoSpin RNA II kit (Macherey-Nagel) according to the manufacturer's instructions. RNA (1 µg) was reverse transcribed using the SuperScript VILO kit (Life Technologies). Quantitative real-time PCR (Q-PCR) was performed with GoTaqR QPCR Master Mix (Promega) in a 25 µl reaction on a thermal cycler (C-1000 Touch; Bio-Rad Laboratories). Product sizes were controlled by DNA gel electrophoresis and the melt curves were evaluated using CFX Manager (Bio-Rad Laboratories). A total of five and four housekeeping genes were selected for their stability in our two cell lines HUVECs and hCMEC/D3, respectively, under our experimental conditions, using the three analytical software programs, geNorm, Normfinder and Bestkeeper (Pfaffl et al., 2004; Vandesompele et al., 2002). We used the relative expression software tool REST-2009 for relative quantification and normalization was achieved by using a normalization factor from all reference genes (Pfaffl et al., 2002). The mean of three technical replicates was calculated per biological replicate. All PCR primer sequences are listed in Table S2.

Cell spreading and immunofluorescence

Transfected cells were trypsinized, treated with 1 mg/ml trypsin inhibitor (Sigma-Aldrich) and incubated in serum-free EBM-2 with 1% BSA for 30 min at 37°C. For achieving a sparse HUVEC density, 10^4 cells were spread for 4 h on 24-well plate slides, coated with 5 µg/ml of FN, in EBM-2 medium containing 5% FN-depleted serum and then fixed with 4% PFA. Confluent HUVECs (2×10^5 cells) were seeded in 24-well plates on slides coated with 20 µg/ml FN and incubated for 72 h in complete supplemented EBM-2 medium. Cells were immunostained as previously described (Faurobert et al., 2013). In brief, cells were fixed with 4% PFA, permeabilized with 0.2% Triton X-100 (when needed), and incubated with appropriate primary antibodies (see list in Table S1). After rinsing, coverslips were incubated with an appropriate Alexa Fluor-conjugated secondary antibody. The cells were mounted in Mowiol/DAPI solution and imaged on confocal Biphoton LSM 510 microscope or epifluorescent Axiomager microscope (Zeiss) with AxioCamMRc (Couleur) camera.

Analysis of adhesive structures, cortical actin area and stress fibers

Images of siRNA-transfected HUVECs spread for 1 h on 5 µg/ml of FN and stained for paxillin phosphorylated at Y118 and actin were acquired using a ApoTome epifluorescence microscope (Zeiss) with AxioCamMRm (N/B). Focal adhesions were quantified by using Matlab (MathWorks, Natick, MA) with an in-house algorithm (available from the corresponding author upon request). Fluorescence cell intensity was first normalized by subtracting the endogenous background. A binary image of all FAs was made by applying a user-dependent intensity threshold. These resulting binary images allowed measurement of two parameters: the total area of focal adhesions per cell and the number of FAs per cell. The position of the cell border was then determined using a hand-draw binary image corresponding to the edge of the cell. To detemine the distribution of FAs, the distance between the centroid of all FAs and each pixel of the cell border was calculated, and the minimal distance was saved. Analysis of number of adhesive structures was made on 20 cells/condition using the following parameters: 1, larger than 0.5 μm^2; 2, larger than 0.5 μm^2 and at more than 5 µm away from the cell border; and 3, smaller than 0.5 μm^2 and at less 2 µm from the cell border. The area of the cortical actin ring of 30–50 round HUVECs spread for 1 h on 5 µg/ml of FN was measured using ImageJ and normalized to the total area of the cell. The results were expressed as a percentage of that seen in the siCT condition. The number of cells with transversal actin fibers above the nucleus was counted on 100 cells per phenotype.

Quantification of the thickness of VE-cadherin junctional staining

Images were acquired on ApoTome epifluorescence microscope (Zeiss) with AxioCamMRm (N/B) at 40× magnification. The surface and length of the junctional VE-cadherin staining for the entire image were measured using the integrated morphometric analysis of MetaMorph application and means were calculated from values of four images per condition (between 40 and 80 cells total). The thickness of VE-cadherin staining was obtained from the ratio of surface to length.

Measurement of VE-cadherin cell surface expression by flow cytometry

Transfected HUVECs were harvested after trypsin treatment and incubated at 37°C for 30 min. Anti-VE-cadherin (BV9 Millipore MABT129) antibody was added to the cell suspension at 1:200 and incubated for 30 min on ice. Cells were washed and labeled with fluorophore-conjugated secondary antibody (Alexa Fluor 647 goat anti-mouse-IgG). VE-cadherin-silenced HUVECs were used as a control for signal specificity. After final wash, cells were fixed in 4% PFA for 10 min on ice, washed in PBS and then analyzed using a flow cytometer (LSR II; BD).

Traction force microscopy

Traction force microscopy experiments were performed using a microscope (Ti-E; Nikon) equipped with an incubator maintaining the temperature at 37°C, mounted with a CCD camera (CoolSNAP; Roper Scientific) and driven with microManager (http://www.micro-manager.org). Cells were imaged with a Nikon 63× air objective lens (NA 1.4). Microbeads used for traction force microscopy were 200-nm Dragon Green beads provided by Bangs Laboratories, Inc. Traction force microscopy calculations were performed as described previously (Hultin et al., 2014; Maruthamuthu et al., 2011). Two images of the beads, before and after cell doublet detachment, and one bright-field image of the cell doublet were recorded. The global shift between the beads was determined by cross-correlation of the images. An in-house Fourier transform traction cytometry (FTTC) algorithm with zeroth-order regularization computed cellular traction forces from the measured substrate displacements (available from the corresponding author upon request). These are determined from images of fluorescent beads

embedded inside the gel network with and without the adherent cell doublet. After correction for experimental drift, fluorescent beads are tracked to obtain a displacement field with high spatial resolution. The final displacement field is obtained on a regular grid with 0.84-µm spacing by linear interpolation. Force reconstruction was conducted with the assumption that the substrate is a linear elastic half-space. The force transmitted at a single cell–cell contact between doublets of cells was determined by calculating the balance of traction forces exerted on the extracellular matrix as previously introduced (Hultin et al., 2014; Maruthamuthu et al., 2011).

Permeability assay

The xCELLigence real-time cell analyzer (RTCA) system (Ozyme) was used to measure electrical impedance over time. Changes in impedance of confluent endothelial cells reflect changes in barrier function (Twiss et al., 2012). 10^5 transfected HUVECs were seeded at confluency in EGM-2 complete medium in wells of E-plates 16 (at least four wells per condition) previously coated with 10 µg/ml vitronectin and 50 µg/ml collagen I. After 2.5 h of adhesion, cells were starved in serum and cultured in basal EBM-2 containing 0.3% BSA for another 24 h. The cell index was normalized to the time of serum starvation to eliminate the signal due to cell spreading and adhering to the substrate.

Zebrafish handling and oocyte injections

Zebrafish handling was performed in compliance with German and Brandenburg state law, carefully monitored by the local authority for animal protection (LAVG). *Krit1/ccm1*^{ty219c} (Chen et al., 1996) and Tg(*kdrl:EGFP*)^{s843} (Jin et al., 2005) zebrafish lines were used. Embryos were injected with antisense oligonucleotide morpholino (MO) (Gene Tools, LLC, Eugene, Oregon) as follows: *rock1*-i1e2MO (MO1; 5′-ACTGTCCTGAAATAAGAAGACAAAT-3′) at 8 ng per embryo for high doses and 5 ng per embryo for low doses, and *rock1*-e2i2MO (MO2; 5′-AGTTCAAGAAGAAAAGCTTACATCT-3′) injected at 3 ng per embryo for high doses and 0.5–1 ng at low doses. Translational blocking morpholinos *rock2a*-ATG-MO (*rock2a*-MO; 5′-TTCTCTCCGCTCCTA-GCGACATTTT-3′) and *rock2b*-ATG-MO (*rock2b*-MO) (5′-TTGCGGC-AGCTCGGTGTCCTTAA-3′) were injected at 2.5 ng per embryo, respectively. Embryos were injected at the one-cell stage and incubated at 28°C in E3 medium supplied with 0.003% phenyl-2-thiourea. The efficacy of gene knockdown was confirmed by western blotting using anti-ROCK1 mouse mAb (ab85305, Abcam) and anti-ROCK2 rabbit pAb (ab228000, Abcam). Embryos were fixed at 48–52 hpf in 4% PFA and 0.01% glutaraldehyde in PBS and stained with Rhodamine–phalloidine (1:250, R415 Thermofisher). The common cardinal vein (CCV) was dissected, flat-mounted in SlowFade Gold Antifade Reagent (S36936, ThermoFisher) and the endothelial cells were imaged with a Zeiss LSM 710 or LSM 780 confocal scanning microscope. Hearts were stained with anti-Alcam (1:20, ZN-8, DSHB) as previously described (Donat et al., 2018) and imaged dissected and flat mounted in SlowFade Gold Antifade Reagent or whole-mount embedded in 1% low-melting agarose with a Zeiss LSM 710 or LSM 780 confocal scanning microscope.

Quantification of cortical versus stress fiber actin levels in zebrafish endothelial cells

The levels of F-actin from two independent MO injections of separate zebrafish cohorts was quantified in three to five embryos per condition with two to nine cells per embryo, yielding indicated final cell numbers, using ImageJ (NIH). *Kdrl*:EGFP marker was utilized to identify the endothelial cells of interest within the zebrafish CCV also served as a marker of cell–cell borders and the cortical actin region. Rhodamine–phalloidin was utilized to label F-actin. Briefly, the *Krdl:*EGFP signal was outlined and then expanded by 10% to incorporate all of the cortical actin signal and this area was defined as cortical actin region. The rest of the intracellular F-actin signal beyond the defined cortical actin region, going towards the center of the cell, was considered as stress fiber actin region. F-actin intensity was normalized to background intensity of each image and results were presented as the fold difference of mean fluorescence intensity of actin within the cortical region to that of F-actin within the stress fiber actin region for each cell. The final presented ratios were further normalized to the WT zebrafish ratio, thereby values below 1 indicate enrichment of stress fiber actin over the WT condition, while those above 1 indicate enrichment of cortical actin over the WT condition.

Statistical tests

Results were assessed by either performing the Tukey's or Dunnett's multiple comparison tests post-ANOVA to control or as otherwise annotated; a 0.5 alpha level was used for all comparisons. Prism software was used to conduct the statistical analysis of all data. $P<0.05$ was considered to be significant. $^*P<0.05$, $^{**}P<0.05$, $^{***}P<0.005$. *n* represents biological replicates.

Acknowledgements

We thank Pierre-Olivier Couraud (Inserm U1016, Institut Cochin, Paris, France) for providing the hCMEC/D3 cell line. We thank C. Guilluy for critically reading the manuscript. We thank A. Grichine and J. Mazzega for their technical assistance, A. Kawska for iconography and M. Fanton d'Andon for helpful discussions.

Competing interests

The authors declare no competing or financial interests.

Author contributions

Conceptualization: J.L., O.D., S.A.-S., C.A.-R., E.F.; Methodology: S.M., Y.A.M., M.B.; Software: R.D.M., M.B.; Validation: J.L., C.J.R., Y.A.M., E.F.; Formal analysis: J.L., Y.A.M., C.B., M.B., E.F.; Investigation: J.L., C.J.R., S.M., Y.A.M., E.P., H.M., E.F.; Resources: H.-H.L., G.B., E.T.-L.; Writing - original draft: C.J.R., S.A.-S., E.F.; Writing - review & editing: J.L., C.J.R., Y.A.M., C.B., E.P., R.D.M., O.D., H.M., G.B., E.T.-L., S.A.-S., C.A.-R., E.F.; Visualization: J.L., C.J.R., Y.A.M., E.F.; Supervision: S.A.-S., E.F.; Project administration: S.A.-S., C.A.-R., E.F.; Funding acquisition: S.A.-S., C.A.-R., E.F.

Funding

C.A.-R. was supported by the Agence Nationale de la Recherche (ANR), by the Ligue Contre le Cancer (LNCC) for Equipe labellisée Ligue 2014 and by Fondation pour la Recherche Médicale (FRM) for Equipe Labellisée. E.F. was supported by the Fondation ARC and by the Ligue Régionale contre le Cancer. J.L was funded by LNCC and FRM. Y.A.M. was funded by the Whitaker Foundation Postdoctoral Scholarship. S.A.-S. has been supported by the excellence cluster REBIRTH, SFB958, and by Deutsche Forschungsgemeinschaft (projects SE2016/7-2 and SE2016/10-1).

Supplementary information

Supplementary information available online at
http://jcs.biologists.org/lookup/doi/10.1242/jcs.216093.supplemental

References

Albiges-Rizo, C., Frachet, P. and Block, M. R. (1995). Down regulation of talin alters cell adhesion and the processing of the alpha 5 beta 1 integrin. *J. Cell Sci.* **108**, 3317-3329.

Amado-Azevedo, J., Valent, E. T. and Van Nieuw Amerongen, G. P. (2014). Regulation of the endothelial barrier function: a filum granum of cellular forces, Rho-GTPase signaling and microenvironment. *Cell Tissue Res.* **355**, 557-576.

Béraud-Dufour, S., Gautier, R., Albiges-Rizo, C., Chardin, P. and Faurobert, E. (2007). Krit 1 interactions with microtubules and membranes are regulated by Rap1 and integrin cytoplasmic domain associated protein-1. *FEBS J.* **274**, 5518-5532.

Borikova, A. L., Dibble, C. F., Sciaky, N., Welch, C. M., Abell, A. N., Bencharit, S. and Johnson, G. L. (2010). Rho kinase inhibition rescues the endothelial cell cerebral cavernous malformation phenotype. *J. Biol. Chem.* **285**, 11760-11764.

Burnette, D. T., Shao, L., Ott, C., Pasapera, A. M., Fischer, R. S., Baird, M. A., Der Loughian, C., Delanoe-Ayari, H., Paszek, M. J., Davidson, M. W. et al. (2014). A contractile and counterbalancing adhesion system controls the 3D shape of crawling cells. *J. Cell Biol.* **205**, 83-96.

Burridge, K. and Wittchen, E. S. (2013). The tension mounts: stress fibers as force-generating mechanotransducers. *J. Cell Biol.* **200**, 9-19.

Chen, J. N., Haffter, P., Odenthal, J., Vogelsang, E., Brand, M., van Eeden, F. J., Furutani-Seiki, M., Granato, M., Hammerschmidt, M., Heisenberg, C. P. et al. (1996). Mutations affecting the cardiovascular system and other internal organs in zebrafish. *Development* **123**, 293-302.

Chu, L.-T., Fong, S. H., Kondrychyn, I., Loh, S. L., Ye, Z. and Korzh, V. (2012). Yolk syncytial layer formation is a failure of cytokinesis mediated by Rock1 function in the early zebrafish embryo. *Biol. Open* **1**, 747-753.

Chuang, H.-H., Liang, S.-W., Chang, Z.-F. and Lee, H.-H. (2013). Ser1333 phosphorylation indicates ROCKI activation. *J. Biomed. Sci.* **20**, 83.
Citi, S., Spadaro, D., Schneider, Y., Stutz, J. and Pulimeno, P. (2011). Regulation of small GTPases at epithelial cell-cell junctions. *Mol. Membr. Biol.* **28**, 427-444.
Crose, L. E., Hilder, T. L., Sciaky, N. and Johnson, G. L. (2009). Cerebral cavernous malformation 2 protein promotes smad ubiquitin regulatory factor 1-mediated RhoA degradation in endothelial cells. *J. Biol. Chem.* **284**, 13301-13305.
Daneshjou, N., Sieracki, N., van Nieuw Amerongen, G. P., Schwartz, M. A., Komarova, Y. A., Malik, A. B. and Conway, D. E. (2015). Rac1 functions as a reversible tension modulator to stabilize VE-cadherin trans-interaction. *J. Cell Biol.* **208**, 23-32.
Donat, S., Lourenco, M., Paolini, A., Otten, C., Renz, M. and Abdelilah-Seyfried, S. (2018). Heg1 and Ccm1/2 proteins control endocardial mechanosensitivity during zebrafish valvulogenesis. *eLife* **7**, e28939.
Faurobert, E. and Albiges-Rizo, C. (2010). Recent insights into cerebral cavernous malformations: a complex jigsaw puzzle under construction. *FEBS J.* **277**, 1084-1096.
Faurobert, E., Rome, C., Lisowska, J., Manet-Dupé, S., Boulday, G., Malbouyres, M., Balland, M., Bouin, A. P., Kéramidas, M., Bouvard, D. et al. (2013). CCM1-ICAP-1 complex controls β1 integrin-dependent endothelial contractility and fibronectin remodeling. *J. Cell Biol.* **202**, 545-561.
Fischer, A., Zalvide, J., Faurobert, E., Albiges-Rizo, C. and Tournier-Lasserve, E. (2013). Cerebral cavernous malformations: from CCM genes to endothelial cell homeostasis. *Trends Mol. Med.* **19**, 302-308.
Fisher, O. S., Deng, H., Liu, D., Zhang, Y., Wei, R., Deng, Y., Zhang, F., Louvi, A., Turk, B. E., Boggon, T. J. et al. (2015). Structure and vascular function of MEKK3–cerebral cavernous malformations 2 complex. *Nat. Commun.* **6**, 7937.
Gibson, C. C., Zhu, W., Davis, C. T., Bowman-Kirigin, J. A., Chan, A. C., Ling, J., Walker, A. E., Goitre, L., Delle Monache, S., Retta, S. F. et al. (2015). Strategy for identifying repurposed drugs for the treatment of cerebral cavernous malformation. *Circulation* **131**, 289-299.
Glading, A. J. and Ginsberg, M. H. (2010). Rap1 and its effector KRIT1/CCM1 regulate beta-catenin signaling. *Dis. Model. Mech.* **3**, 73-83.
Glading, A., Han, J., Stockton, R. A. and Ginsberg, M. H. (2007). KRIT-1/CCM1 is a Rap1 effector that regulates endothelial cell-cell junctions. *J. Cell Biol.* **179**, 247-254.
Hartmann, S., Ridley, A. J. and Lutz, S. (2015). The function of Rho-associated kinases ROCK1 and ROCK2 in the pathogenesis of cardiovascular disease. *Front. Pharmacol.* **6**, 276.
Hogan, B. M., Bussmann, J., Wolburg, H. and Schulte-Merker, S. (2008). ccm1 cell autonomously regulates endothelial cellular morphogenesis and vascular tubulogenesis in zebrafish. *Hum. Mol. Genet.* **17**, 2424-2432.
Hotulainen, P. and Lappalainen, P. (2006). Stress fibers are generated by two distinct actin assembly mechanisms in motile cells. *J. Cell Biol.* **173**, 383-394.
Hultin, S., Zheng, Y., Mojallal, M., Vertuani, S., Gentili, C., Balland, M., Milloud, R., Belting, H. G., Affolter, M., Helker, C. S. et al. (2014). AmotL2 links VE-cadherin to contractile actin fibres necessary for aortic lumen expansion. *Nat. Commun.* **5**, 3743.
Huveneers, S., Daemen, M. J. A. P. and Hordijk, P. L. (2015). Between Rho(k) and a hard place: the relation between vessel wall stiffness, endothelial contractility, and cardiovascular disease. *Circ. Res.* **116**, 895-908.
Iizuka, M., Kimura, K., Wang, S., Kato, K., Amano, M., Kaibuchi, K. and Mizoguchi, A. (2012). Distinct distribution and localization of Rho-kinase in mouse epithelial, muscle and neural tissues. *Cell Struct. Funct.* **37**, 155-175.
Jilkova, Z. M., Lisowska, J., Manet, S., Verdier, C., Deplano, V., Geindreau, C., Faurobert, E., Albigès-Rizo, C. and Duperray, A. D. (2014). CCM proteins control endothelial β1 integrin dependent response to shear stress. *Biol. Open* **3**, 1228-1235.
Jin, S. W., Beis, D., Mitchell, T., Chen, J. N. and Stainier, D. Y. (2005). Cellular and molecular analyses of vascular tube and lumen formation in zebrafish. *Development* **132**, 5199-5209.
Julian, L. and Olson, M. F. (2014). Rho-associated coiled-coil containing kinases (ROCK): structure, regulation, and functions. *Small GTPases* **5**, e29846.
Komarova, Y. and Malik, A. B. (2010). Regulation of endothelial permeability via paracellular and transcellular transport pathways. *Annu. Rev. Physiol.* **72**, 463-493.
Labauge, P., Denier, C., Bergametti, F. and Tournier-Lasserve, E. (2007). Genetics of cavernous angiomas. *Lancet. Neurol.* **6**, 237-244.
Lock, F. E. and Hotchin, N. A. (2009). Distinct roles for ROCK1 and ROCK2 in the regulation of keratinocyte differentiation. *PLoS ONE* **4**, e8190.
Mably, J. D., Chuang, L. P., Serluca, F. C., Mohideen, M.-A. P. K., Chen, J.-N. and Fishman, M. C. (2006). santa and valentine pattern concentric growth of cardiac myocardium in the zebrafish. *Development* **133**, 3139-3146.
Maruthamuthu, V., Aratyn-Schaus, Y. and Gardel, M. L. (2010). Conserved F-actin dynamics and force transmission at cell adhesions. *Curr. Opin. Cell Biol.* **22**, 583-588.
Maruthamuthu, V., Sabass, B., Schwarz, U. S. and Gardel, M. L. (2011). Cell-ECM traction force modulates endogenous tension at cell-cell contacts. *Proc. Natl. Acad. Sci. USA* **108**, 4708-4713.
McDonald, D. A., Shi, C., Shenkar, R., Stockton, R. A., Liu, F., Ginsberg, M. H., Marchuk, D. A. and Awad, I. A. (2012). Fasudil decreases lesion burden in a murine model of cerebral cavernous malformation disease. *Stroke* **43**, 571-574.
Mui, K. L., Chen, C. S. and Assoian, R. K. (2016). The mechanical regulation of integrin-cadherin crosstalk organizes cells, signaling and forces. *J. Cell Sci.* **129**, 1093-1100.
Newell-Litwa, K. A., Badoual, M., Asmussen, H., Patel, H., Whitmore, L. and Horwitz, A. R. (2015). ROCK1 and 2 differentially regulate actomyosin organization to drive cell and synaptic polarity. *J. Cell Biol.* **210**, 225-242.
Pfaffl, M. W., Horgan, G. W. and Dempfle, L. (2002). Relative expression software tool (REST) for group-wise comparison and statistical analysis of relative expression results in real-time PCR. *Nucleic Acids Res.* **30**, e36.
Pfaffl, M. W., Tichopad, A., Prgomet, C. and Neuvians, T. P. (2004). Determination of stable housekeeping genes, differentially regulated target genes and sample integrity: BestKeeper–Excel-based tool using pair-wise correlations. *Biotechnol. Lett.* **26**, 509-515.
Priya, R., Gomez, G. A., Budnar, S., Verma, S., Cox, H. L., Hamilton, N. A. and Yap, A. S. (2015). Feedback regulation through myosin II confers robustness on RhoA signalling at E-cadherin junctions. *Nat. Cell Biol.* **17**, 1282-1293.
Priya, R., Liang, X., Teo, J. L., Duszyc, K., Yap, A. S. and Gomez, G. A. (2017). ROCK1 but not ROCK2 contributes to RhoA signaling and NMIIA-mediated contractility at the epithelial zonula adherens. *Mol. Biol. Cell* **28**, 12-20.
Richardson, B. T., Dibble, C. F., Borikova, A. L. and Johnson, G. L. (2013). Cerebral cavernous malformation is a vascular disease associated with activated RhoA signaling. *Biol. Chem.* **394**, 35-42.
Robertson, J., Jacquemet, G., Byron, A., Jones, M. C., Warwood, S., Selley, J. N., Knight, D., Humphries, J. D. and Humphries, M. J. (2015). Defining the phospho-adhesome through the phosphoproteomic analysis of integrin signalling. *Nat. Commun.* **6**, 6265.
Rubenstein, N. M., Callahan, J. A., Lo, D. H. and Firestone, G. L. (2007). Selective glucocorticoid control of Rho kinase isoforms regulate cell-cell interactions. *Biochem. Biophys. Res. Commun.* **354**, 603-607.
Sander, E. E., ten Klooster, J. P., van Delft, S., van der Kammen, R. A. and Collard, J. G. (1999). Rac downregulates Rho activity: reciprocal balance between both GTPases determines cellular morphology and migratory behavior. *J. Cell Biol.* **147**, 1009-1022.
Schroer, A. K. and Merryman, W. D. (2015). Mechanobiology of myofibroblast adhesion in fibrotic cardiac disease. *J. Cell Sci.* **128**, 1865-1875.
Shenkar, R., Shi, C., Rebeiz, T., Stockton, R. A., McDonald, D. A., Mikati, A. G., Zhang, L., Austin, C., Akers, A. L., Gallione, C. J. et al. (2015). Exceptional aggressiveness of cerebral cavernous malformation disease associated with PDCD10 mutations. *Genet. Med.* **17**, 188-196.
Shenkar, R., Shi, C., Austin, C., Moore, T., Lightle, R., Cao, Y., Zhang, L., Wu, M., Zeineddine, H. A., Girard, R. et al. (2017). RhoA kinase inhibition with fasudil versus simvastatin in murine models of cerebral cavernous malformations. *Stroke* **48**, 187-194.
Shimokawa, H., Sunamura, S. and Satoh, K. (2016). RhoA/Rho-kinase in the cardiovascular system. *Circ. Res.* **118**, 352-366.
Stockton, R. A., Shenkar, R., Awad, I. A. and Ginsberg, M. H. (2010). Cerebral cavernous malformations proteins inhibit Rho kinase to stabilize vascular integrity. *J. Exp. Med.* **207**, 881-896.
Tumusiime, S., Rana, M. K., Kher, S. S., Kurella, V. B., Williams, K. A., Guidry, J. J., Worthylake, D. K. and Worthylake, R. A. (2009). Regulation of ROCKII by localization to membrane compartments and binding to DynaminI. *Biochem. Biophys. Res. Commun.* **381**, 393-396.
Twiss, F., Le Duc, Q., Van Der Horst, S., Tabdili, H., Van Der Krogt, G., Wang, N., Rehmann, H., Huveneers, S., Leckband, D. E. and De Rooij, J. (2012). Vinculin-dependent Cadherin mechanosensing regulates efficient epithelial barrier formation. *Biol. Open* **1**, 1128-1140.
Uhlik, M. T., Abell, A. N., Johnson, N. L., Sun, W., Cuevas, B. D., Lobel-Rice, K. E., Horne, E. A., Dell'Acqua, M. L. and Johnson, G. L. (2003). Rac-MEKK3-MKK3 scaffolding for p38 MAPK activation during hyperosmotic shock. *Nat. Cell Biol.* **5**, 1104-1110.
Vandesompele, J., De Preter, K., Pattyn, F., Poppe, B., Van Roy, N., De Paepe, A. and Speleman, F. (2002). Accurate normalization of real-time quantitative RT-PCR data by geometric averaging of multiple internal control genes. *Genome Biol.* **3**, RESEARCH0034.
Vega, F. M., Fruhwirth, G., Ng, T. and Ridley, A. J. (2011). RhoA and RhoC have distinct roles in migration and invasion by acting through different targets. *J. Cell Biol.* **193**, 655-665.
Wang, G., Cadwallader, A. B., Jang, D. S., Tsang, M., Yost, H. J. and Amack, J. D. (2011). The Rho kinase Rock2b establishes anteroposterior asymmetry of the ciliated Kupffer's vesicle in zebrafish. *Development* **138**, 45-54.
Weksler, B. B., Subileau, E. A., Perriere, N., Charneau, P., Holloway, K., Leveque, M., Tricoire-Leignel, H., Nicotra, A., Bourdoulous, S., Turowski, P. et al. (2005). Blood-brain barrier-specific properties of a human adult brain endothelial cell line. *FASEB J.* **19**, 1872-1874.

Whitehead, K. J., Chan, A. C., Navankasattusas, S., Koh, W., London, N. R., Ling, J., Mayo, A. H., Drakos, S. G., Jones, C. A., Zhu, W. et al. (2009). The cerebral cavernous malformation signaling pathway promotes vascular integrity via Rho GTPases. *Nat. Med.* **15**, 177-184.

Wimmer, R., Cseh, B., Maier, B., Scherrer, K. and Baccarini, M. (2012). Angiogenic sprouting requires the fine tuning of endothelial cell cohesion by the Raf-1/Rok-alpha complex. *Dev. Cell* **22**, 158-171.

Yadla, S., Jabbour, P. M., Shenkar, R., Shi, C., Campbell, P. G. and Awad, I. A. (2010). Cerebral cavernous malformations as a disease of vascular permeability: from bench to bedside with caution. *Neurosurg. Focus* **29**, E4.

Yamada, S. and Nelson, W. J. (2007). Localized zones of Rho and Rac activities drive initiation and expansion of epithelial cell-cell adhesion. *J. Cell Biol.* **178**, 517-527.

Yoneda, A., Multhaupt, H. A. B. and Couchman, J. R. (2005). The Rho kinases I and II regulate different aspects of myosin II activity. *J. Cell Biol.* **170**, 443-453.

Zhang, H. and Labouesse, M. (2012). Signalling through mechanical inputs: a coordinated process. *J. Cell Sci.* **125**, 3039-3049.

Zhou, Z., Tang, A. T., Wong, W.-Y., Bamezai, S., Goddard, L. M., Shenkar, R., Zhou, S., Yang, J., Wright, A. C., Foley, M. et al. (2016). Cerebral cavernous malformations arise from endothelial gain of MEKK3-KLF2/4 signalling. *Nature* **532**, 122-126.

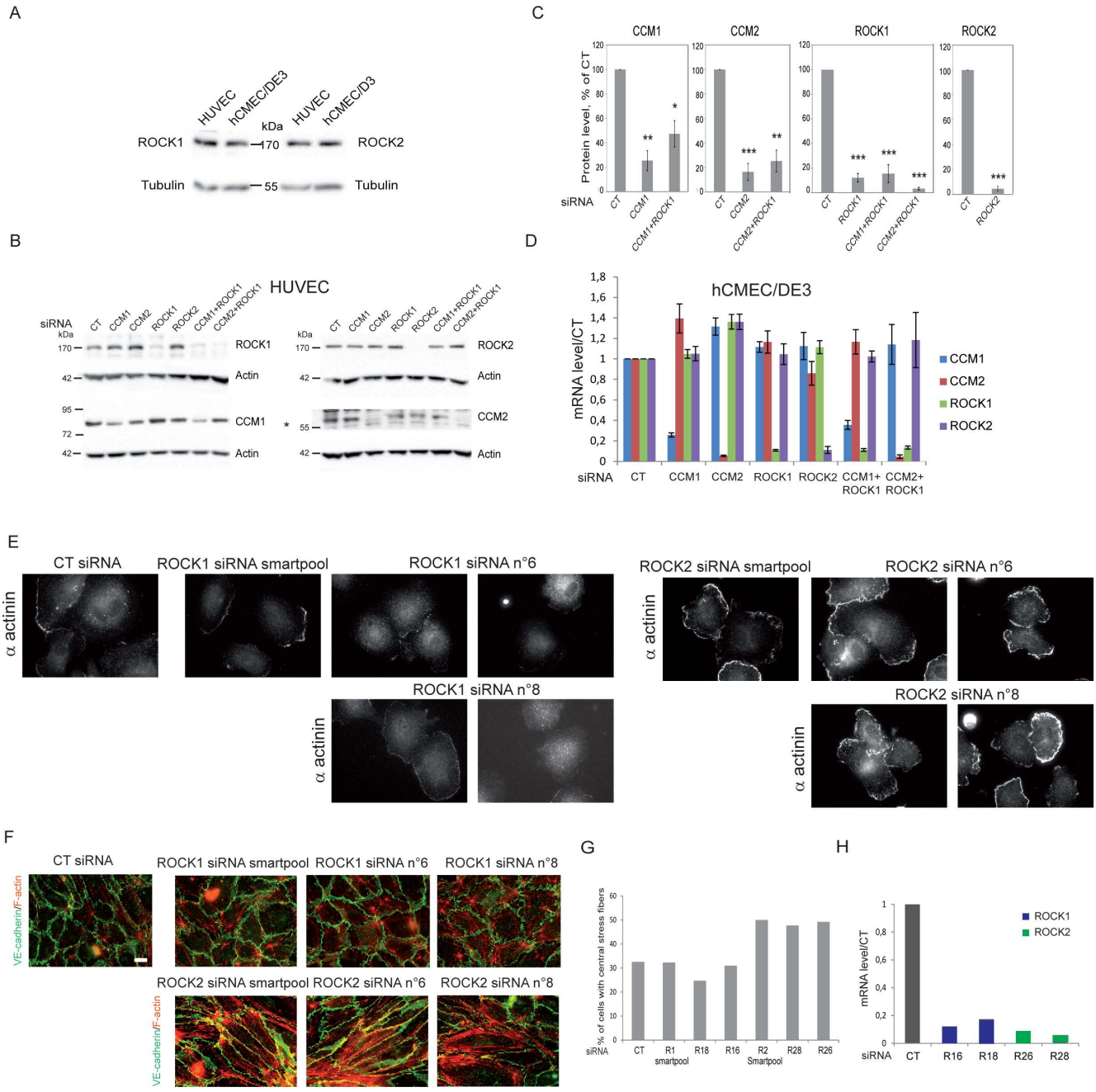

Figure S1: Efficiency of siRNA silencing in endothelial cells. (A) Representative immunoblot of the ROCK1 and ROCK2 protein content in total lysates from confluent HUVEC and hCMEC/D3. (B) Representative immunoblot images of CCM1, CCM2, ROCK1 and ROCK2 protein content in HUVEC transfected with smartpool siRNA * marks CCM2 band. (C) Histograms represent mean values of remaining protein content normalized to CT. Error bars, s.e.m (n=5). (D) CCM1, CCM2, ROCK1 and ROCK2 mRNA levels in siRNA-transfected hCMEC/D3 normalized to CT. Error bars, s.e.m (n=3), *P<0,05; **P<0,005; ***P<0,0005 (One-Way ANOVA with Dunnett's multiple comparison test). (E) Representative images of α actinin staining of silenced HUVEC with individuals siRNA targeting ROCK1 and ROCK2 and spread for 1h on FN at 2 µg/ml. (F) Representative images of VE-cadherin, F-actin and merge stainings of monolayers of HUVEC silenced with individual siRNA targeting ROCK1 and ROCK2 after 72 h of culture. (G) Quantification of the percentage of cells displaying central actin stress fibers when spread for 1h on FN 2 µg/ml. (H) Efficiency of silencing of individual siRNA normalized to CT.

Journal of Cell Science • Supplementary information

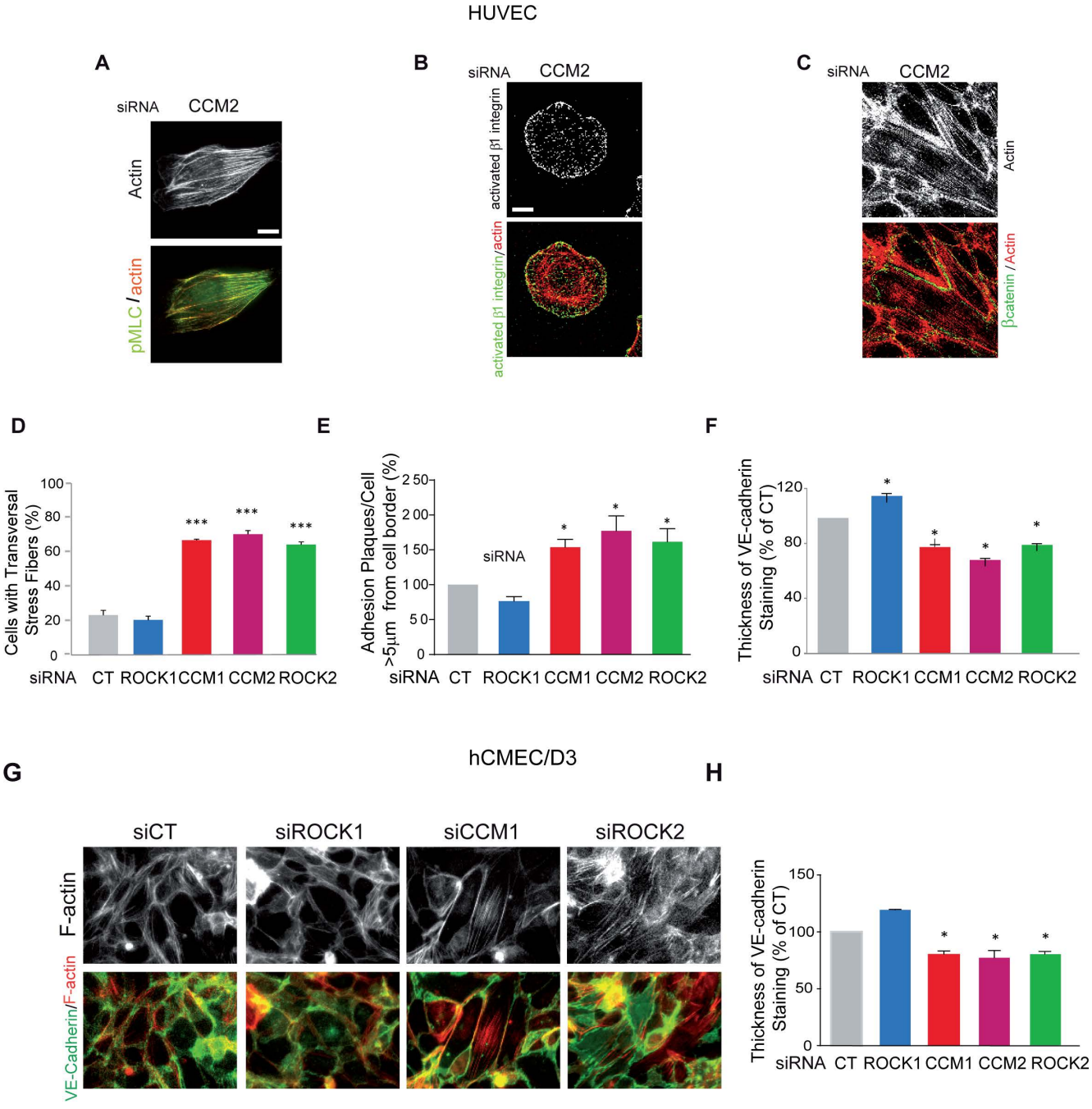

Figure S2: **CCM2 loss as CCM1 loss impairs cell adhesions and actomyosin cytoskeleton organization in HUVEC and hCMEC/D3**.

(A) Representative immunofluorescence images of F-actin (grey) and merged images with pMLC in sparse HUVEC depleted for CCM2 performed after 4h of adhesion on 5µg/ml FN. (B) Representative immunofluorescence images of β1 integrin (green) and F-actin (red) performed after 1h of adhesion on 5µg/ml FN. Representative immunofluorescence images of F-actin and merged images with β-catenin performed after 72h of culture on 20µg/ml FN for HUVEC (C) and hCMEC/D3 (G) respectively. (D) Quantification of the percentage of cells expressing stress fibers. Error bars, s.e.m. (n=4) (E) Quantification of the percentage of adhesion plaques per cell larger than 0.5 μm^2 at more than 5 µm from the cell border. Error bars, s.d (n=2) (F) Quantification of the thickness of VE-cadherin staining. Error bars, s.e.m (n=4). * $P < 0.05$; **P<0,005; ***P<0.0005. (One-way ANOVA with Dunnett's multiple comparisons post-test). (D-F) Parts of these bar graphs are the same as in Fig. 1.

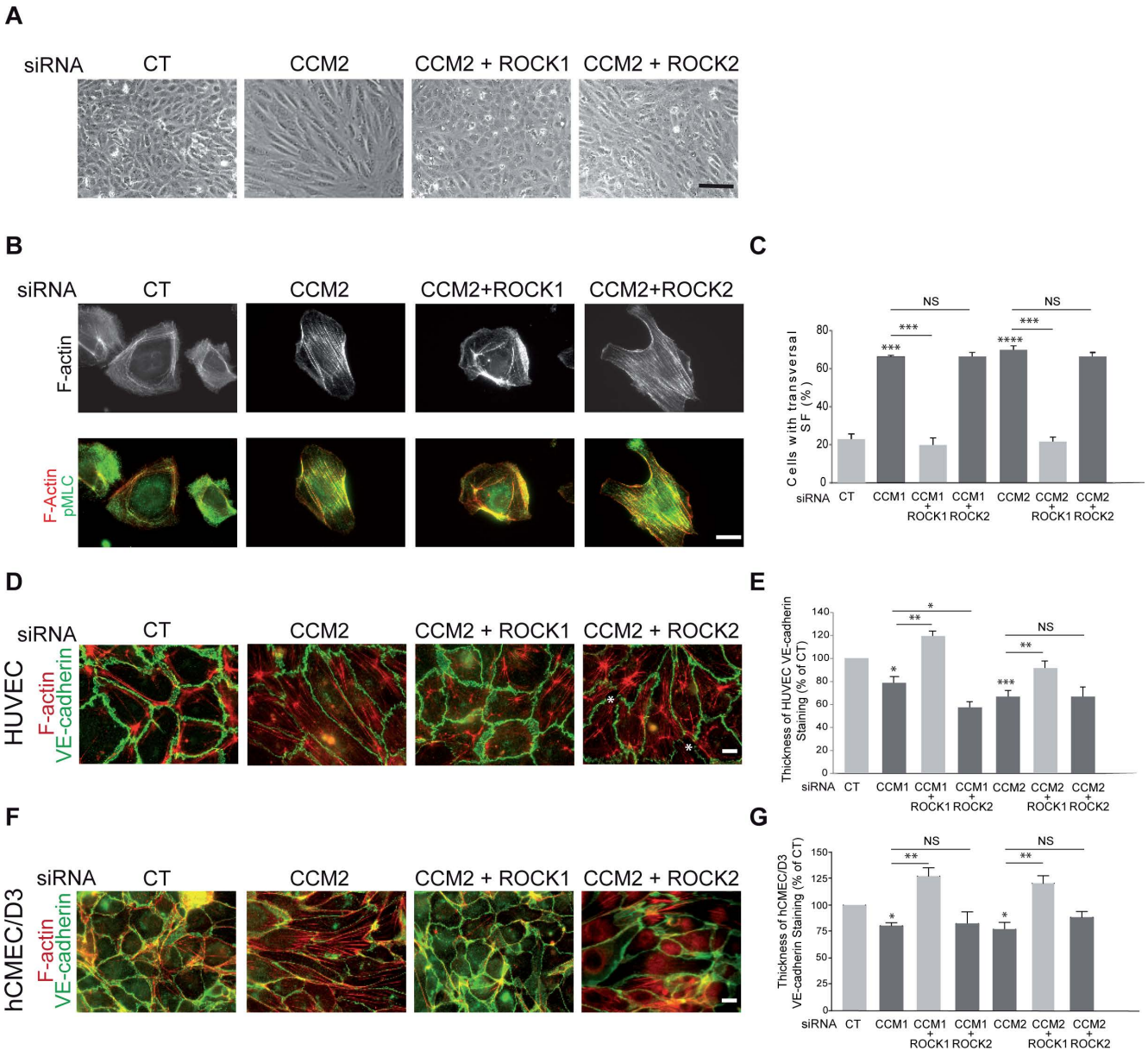

Figure S3: ROCK1 silencing restores normal adhesive and contractile phenotypes in CCM2-depleted HUVEC.

(A) Representative phase contrast images of siRNA transfected HUVEC cell monolayers. Scale bar 50 µm. (B) Representative immunofluorescence of sparse siRNA transfected HUVEC stained for F-actin (grey) and merged images with pMLC (scale bar 10µm). (C) Percentage of cells with transversal SF. Error bars, s.e.m (n=4 except for CCM2+ROCK2 n=2). (D) Representative immunofluorescence of F-actin (grey) and merged images with VE-cadherin of HUVEC monolayers on 20µg/ml FN coated coverslips 72 hours post plating. Scale bar 10µm. * indicates zone of detachment of intercellular junctions. (E) Quantifications of VE-cadherin thickness from immunofluorescence staining of HUVEC presented as percentage of CT. Errors bar, s.e.m (n=4 except for CCM2+ROCK1 n=3 and CCM2+ROCK2 n=2). * P< 0.05, **P<0.005, ***P<0.0005. (One-way ANOVA with Dunett's multiple comparisons to CT or otherwise annotated). Parts of the bar graphs in (C) (E) (G) are the same as in Fig. 3.

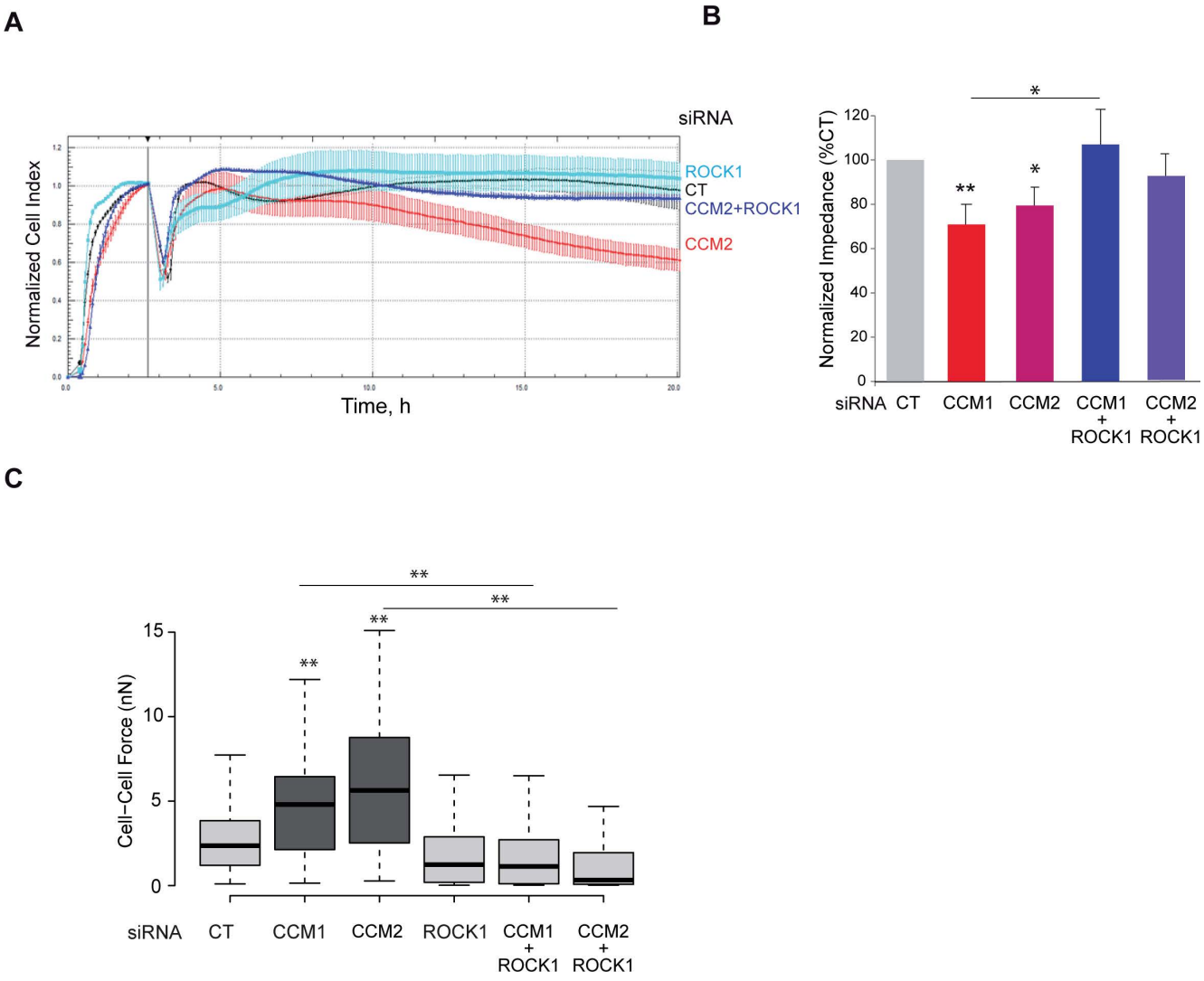

Figure S4: ROCK1 silencing restores functional permeability barrier in CCM2-depleted HUVEC and intercellular tensile forces.

(A) Representative kinetics of the impedance of silenced HUVEC monolayers (cell indexes were normalized at serum starvation). (B) Bar graph quantification of the plateau value of normalized impedance after 25h. Error bars, s.e.m (n=6) (C) Cell-cell forces measurement from traction force microscopy of HUVEC doublets plated on top of 5 kPa FN-coated polyacrylamide gel. Between 45 and 80 doublets were analyzed (n=4). One-way Anova with Dunnett's multiple comparisons test. * $p<0.05$, ** $p<0,001$. (B) (C) Part of these bar graphs are the same as in Fig. 4.

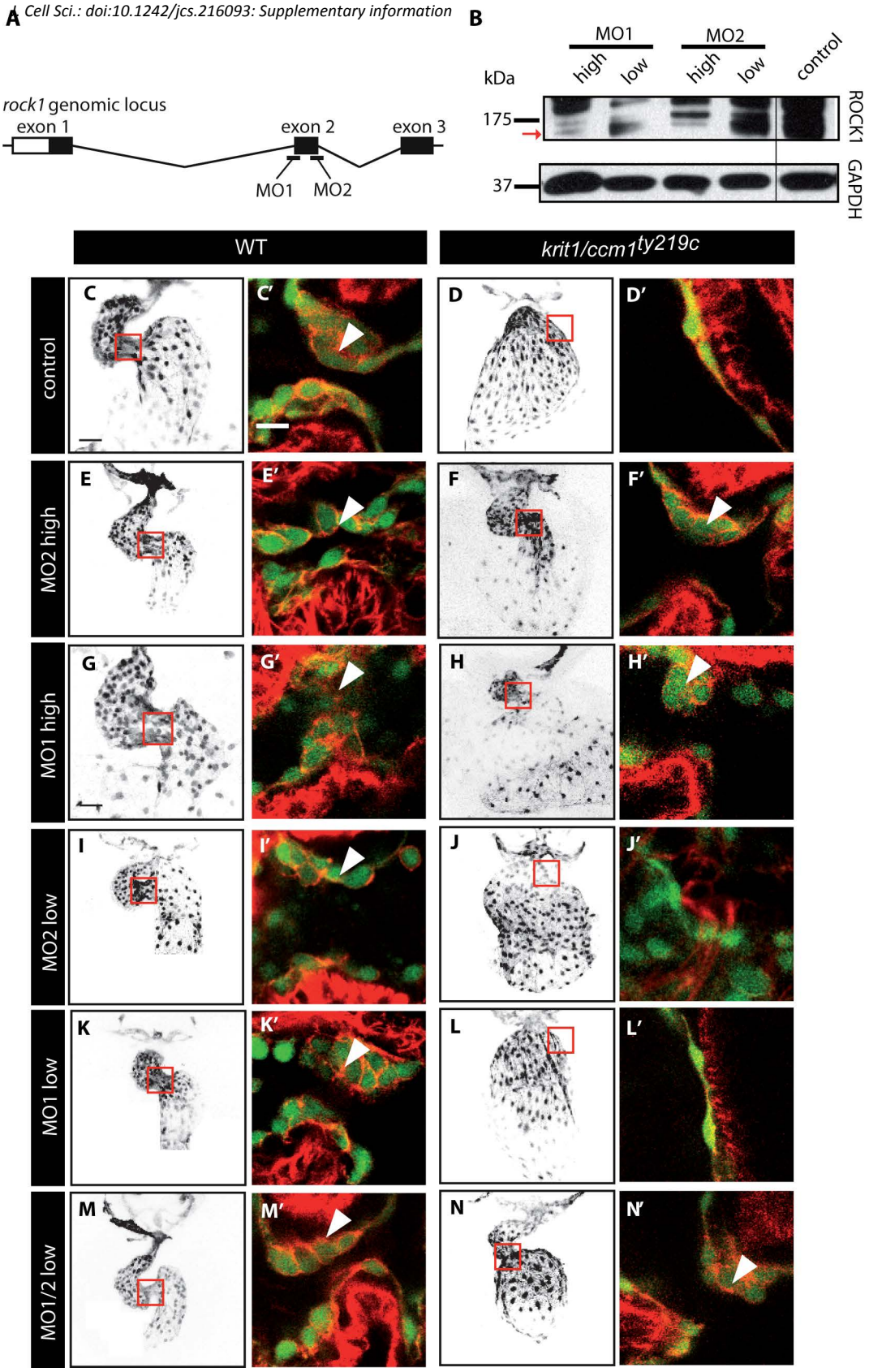

Figure S5: Representative images for rock1 morpholino mediated rescue of *krit1/ccm1^{ty219c}*.

(A) Gene structure of zebrafish *rock1* and target sites of two antisense oligonucleotide morpholinos, MO1 and MO2. (B) Representative immunoblot showing levels of Rock1 protein and Gapdh from control and high doses of rock1-MO1 and rock1-MO2 treated WT embryos at 48 hpf for which Rock1 band is indicated by a red arrow. (C, C'-D, D') Control for WT and *ccm1^{ty219c}* zebrafish hearts at 48 hpf. Injected embryos with high morpholino doses of MO1 and MO2, that have been used for F-actin quantifications, show rescue cardiac morphology (F,H) and endocardial cushion formation (F', H') in *ccm1^{ty219c}* mutants. (E, E', G, G') Atrioventricular canal is still formed under high morpholino doses in WT hearts. (I, I', J, J', K, K', L, L') Low doses of MO1 and MO2 do not change cardiac morphology nor atrioventricular canal formation, neither in WT, nor in the *ccm1^{ty219c}* mutants. However, combined injection of low doses of MO1 and MO2 restores cardiac morphology (N) and endocardial cuboidal cell shape (N') in *ccm1^{ty219c}* mutants as compared to WT (M, M'). Scale bars, 50 µm in C-N and 10 µm in C'-N'.

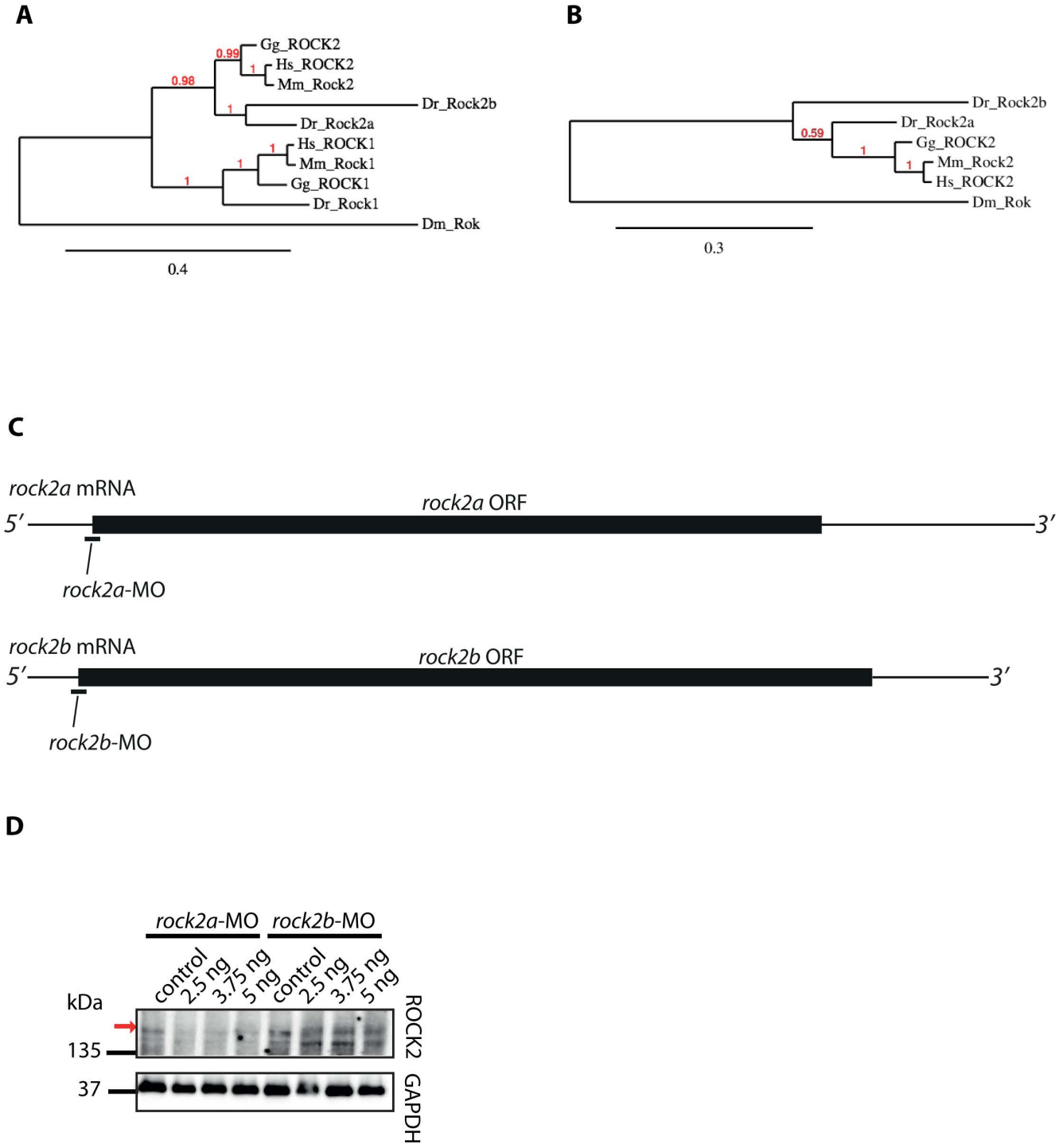

Figure S6: (A) Phylogenetic analysis of different ROCK1 and ROCK2 protein sequences. Zebrafish Rock1 (Dr_Rock1) clusters together with ROCK1, whereas zebrafish Rock2a (Dr_Rock2a) and Rock2b (Dr_Rock2b) cluster together with ROCK2 protein sequences. (B) An independent phylogenetic analysis with only ROCK2 sequences reveals that Rock2b is more derived than Rock2a and forms an sister branch to all other ROCK2 sequences. In both phylogenetic analyses Drosophila ROCK (Dm_Rok) was uses as an outgroup. (C) Schematic overview of mRNAs of *rock2a* and *rock2b* and target sites of oligonucleotide morpholinos, *rock2a*-MO and *rock2b*-MO, respectively. (D) Representative immunoblot showing levels of Rock2a/Rock2b protein and GAPDH from control and morpholino-injected embryos at 24 hpf.

Supplementary table1.

List of antibodies used

Antibody	reactivity	clone	Reference, supplier	Use and dilution
CCM2 rabbit pAB	human	-	AP26022PU-N Interchim (Acris),	WB: 1/500
HUTS-4 mouse mAb	human, rat	-	MAB2079Z Milipore	IF: 1/100
pPaxilinY118 rabbit pAb	human, mouse	-	44-722G Invitrogen	IF: 1/200
β - catenin mouse mAb	human, canine	6F9	C7082 Sigma	WB: 1/2000, IF: 1/500
Zyxin mouse mAb	human, mouse, rat	164D4	307011 Synaptic Systems	IF: 1/100
ROCK 1 mouse mAb	human, mouse, rat	-	611136 BD Pharmingen	WB: 1/250
ROCK 1 mouse mAb	mouse, human	-	ab58305 Abcam	WB: 1/1000
ROCK1 rabbit	human, mouse, rat	EPR638Y	04-1121 Millipore	IP: 4ug of Ab/1 mg of total protein
ROCK 2 mouse mAb	human, mouse, rat	-	610623 BD Pharmingen	WB: 1/2000
ROCK 2 rabbit pAb	human, mouse, rat	-	a715985Abcam	WB: 1/2000
ROCK 2 goat pAb	human, mouse, rat	C-20	sc-1851 Santa Cruz	IP: 4ug of Ab/1mg of protein
Actin mouse mAb	mouse, human	AC-40	A3853 Sigma	WB: 1/2000

β-Tubulin mouse mAb	mouse, human	Tub 2.1	T4026 Sigma	WB: 1/2000
pMLC 2 (Ser 19) rabbit pAb	human, mouse, rat	-	3671 Cell Signaling Technology	IF: 1/50
pMYPT1 (Thr696) rabbit pAb	human, mouse	-	ABS45 Millipore	WB: 1/1000
TRITC phalloidin	-	-	P-1951 Sigma-Aldrich	IF 1/1000
Atto 647 N phaloidin	-	-	65906 Sigma (Fluka)	IF 1/2000
Alexa 488 phaloidin	-	-	A12379 Life Technologies	IF 1/2000
Goat IgG *HRP	mouse	-	115-036-003 Jackson Immunoresearch	WB:1/20000
Rabbit IgG*HRP	donkey	-	711-036-152 Jackson Immunoresearch	WB: 1/10000
Goat IgG* Alexa Fluor 647	mouse	-	A-21236 Life Technologies	IF: 1/1000
Goat IgG* Alexa Fluor 546	mouse	-	A-11030, Invitrogen	IF: 1/1000
Goat IgG* Alexa Fluor 488	rabbit	-	A-11034, Invitrogen,	IF: 1/500
Goat IgG* Alexa Fluor 546	rabbit	-	A-11035, Invitrogen	IF: 1/1000
IgG control rabbit	human	-	I2011 Sigma	IP: 4ug/ 1mg of protein
IgG control goat	human	-	Sigma M5899	IP: 4ug/ 1mg of protein

Supplementary table 2:

RT-PCR primers used

House-keeping genes

Gene symbol	Gene name	Accession number	sequence	Efficiency
ACTB	β-Actin	NM_001101	5' TGACGTGGACATCCGCAAAG 3' 5' CTGGAAGGTGGACAGCGAGG 3'	98%
TBP	TATA box binding portein	NM_003194	5' GAGAGTTCTGGGATTGTACCG 3' 5' ATCCTCATGATTACCGCAGC 3'	90%
HPRT1	Hypoxanthine phosphoribosyl-transferase 1	NM_000194	5' GACCAGTCAACAGGGGACAT 3' 5' CCTGACCAAGGAAAGCAAAG 3'	104%
RPLP0	Ribosomal protein Large P0	NM_001002	5' TGCTCAACATCTCCCCCTTCTC 3' 5' ACTGGCAACATTGCGGACAC 3'	105%
ATP50	ATP synthase, H+ transporting, mitochondrial F1 complex, O subunit	NM_001697	5' ATTGAAGGTCGCTATGCCACAG 3' 5' AACAGAAGCAGCCACTTTGGG 3'	90%
RANbp2	RAN binding protein 2	NM_006267	5' TGTAGTGATACTGATGAAGACAATGG 3' 5' TTGTGCTAGTTATTTCTTCTGTCTGAG 3'	88%

Target genes:

Target gene	Accession number	sequence	Efficiency
CCM1	NM_194456	5' gaagcgcctgtgaaggagattc 3' 5' acaatatgcgagtggcctcaac 3'	97%
CCM2	NM_001029835	5' cctgcacagcgatgactct 3' 5' accacccacatccacagatt 3'	96%
ROCK1	NM_005406	5' aaagaaaggatggaggatgaagt 3' 5' tgtaacaacagccgcttatttg 3'	98%
ROCK2	NM_004850	5' cccatcaacgtggagagc 3' 5' aagcaggaaaatctaaatcaagga 3'	89%